# A simplified modelling approach for thermal behaviour analysis in hybrid plasma arc-laser additive manufacturing

Chong Wang, Yongle Sun, Guangyu Chen, Xin Chen*, Jialuo Ding, Wojciech Suder, Chenglei Diao, Stewart Williams

*Welding Engineering and Laser Processing Centre, Cranfield University, Bedfordshire, MK43 0AL, UK*

## ARTICLE INFO

## ABSTRACT

Hybrid plasma transferred arc (PTA)-laser additive manufacturing (AM) has the potential to build large-scale metal components with high deposition rate and near-net shape. However, the process is complex with many parameters adjustable for process control, which determine the thermal behaviour and thus the final structure and properties of the deposited components. In this study, a three-dimensional steady-state finite element model with two independent circular surface heat sources was developed, validated, and used to analyse the thermal behaviour in hybrid PTA-laser AM of Ti-6Al-4V. Artificial conductivity in three orthogonal directions was applied in the melt pool to compensate for the melt pool convection effect. The predicted melt pool geometry, heat-affected zone and thermal cycles had good agreement with the corresponding experimental data. This model has advantages over the widely used volumetric heat source model, since it is more representative of the energy sources used, giving accurate thermal prediction for a wide range of process parameters. As the heat source parameters in this model are directly linked to the actual arc/laser size, it enables to capture heat source size effect on the hybrid process. In addition, it is easier to calibrate compared to the model with volumetric heat sources due to the fewer empirical parameters involved. It was found that in the investigated ranges of all the parameters, the melt pool geometry is more sensitive to laser power and travel speed compared to arc-laser separation distance and laser beam size. The full-field distributions of the cooling rate and temperature gradient in the hybrid process were obtained and the roles that different process parameters played on them were also studied, which provided useful thermal information for metallurgical analysis.

© 2022 The Author(s). Published by Elsevier Ltd.
This is an open access article under the CC BY license (http://creativecommons.org/licenses/by/4.0/)

## 1. Introduction

Additive manufacturing (AM) is a transformative approach to producing industrial parts, which offers unrivalled benefits in comparison with traditional subtractive manufacturing, such as low material waste, short lead-time, and high design flexibility [1]. There are three main types of heat sources used for metal AM, which are laser [2,3], electron beam [4,5], and electric arc [6–8]. Each of them offers a different set of benefits and challenges [9]. For example, arc-based processes have relatively high efficiency and deposition rate, whilst laser-based processes are well known for their high controllability. Hybrid arc-laser AM was developed to combine the advantages of both an electric arc and laser, which has the potential to achieve both high deposition rate and near-net shape [9,10]. In hybrid arc-laser AM, the structure and properties

of the deposited components are determined by the thermal behaviour of the material, such as melt pool geometry and thermal history. For example, the generated melt pool plays a significant role in determining the deposited bead shape and consequently the surface finish of the final parts [7]. The thermal history governs the microstructural evolution, which considerably affects the mechanical properties [11]. Therefore, in order to build a defect-free and structurally sound component, the hybrid AM process needs to be controlled precisely by appropriate selection of different process parameters, such as travel speed, laser power, laser beam size, and the relative position of the two heat sources, to achieve a desired thermal condition of the material.

Compared to AM processes with a single heat source, the hybrid arc-laser process is more complicated owing to a greater number of process variables. Therefore, it is time-consuming and expensive to select different variables by trial and error. Moreover, accurately measuring the global thermal conditions during deposition is quite challenging. Finite element (FE) modelling has been

* Corresponding author.
  *E-mail address:* x.chen1@cranfield.ac.uk (X. Chen).

demonstrated to be an effective way to provide detailed information on the thermal behaviour for metal AM processes. For example, Xiong et al. [12] built a three-dimensional (3D) FE model to investigate the effect of substrate preheating on the thermal behaviour in wire + arc additive manufacturing (WAAM). They found that substrate preheating resulted in a smoother thermal cycle and led to a decrease in the cooling rate of the melt pool. The thermal behaviour as a function of different variables in powder bed fusion (PBF) process has also been studied using an FE model [13–15]. However, these models are based on transient analysis, which still require relatively long computational time. Most importantly, in many AM processes, apart from the initiation and termination of a deposit, steady-state conditions are reached quickly due to the long deposition time and constant travel speed that is often used. Therefore, a steady-state FE model can be used in many cases and will be effective in greatly reducing the computational time. Ding et al. [16] built a 3D steady-state FE model for WAAM and reported that it saved more than 99% computational time in the thermal analysis compared to the transient model without compromising the accuracy. Such a steady-state FE model could be potentially used as a process control tool to efficiently predict the thermal conditions needed for a particular structure and property.

So far, most of the hybrid arc-laser configurations have been used for welding applications [17–19]. However, the purpose of using the hybrid configuration in welding is different from that in AM, leading to different optimum process conditions. In hybrid arc-laser welding, the laser with a small beam size in keyhole regime is normally used to increase the weld penetration, whilst the arc is used to enhance the gap-filling capability, which consequently improves the welding efficiency as well as the process tolerance. Also, in some gas metal arc (GMA) welding cases, a laser is used to stabilise the arc thus to improve the process stability and weld quality [20]. Therefore, the separation distance between the arc and laser in hybrid welding needs to be very close to ensure their synergic effect (normally less than the sum of arc radius and laser beam radius) [17]. In hybrid AM, by contrast, the arc is used to melt the feedstock efficiently and generate the melt pool, whilst the laser is used to control the melt pool size precisely [9,10]. In addition, a flat bead profile with low penetration is favourable in AM to achieve good surface finish and high process efficiency [7,9]. Therefore, a laser in the conduction regime is desired for the hybrid arc-laser AM process, and the separation distance between the two heat sources is relatively long (normally more than the sum of arc radius and laser beam radius).

Due to the short arc-laser separation distance and high penetration depth, a combined volumetric heat source model or two separate volumetric heat source models with very close distance are normally used to simulate the thermal conditions in hybrid arc-laser welding. For example, Chen et al. [21] used a combined volumetric heat source model (double ellipsoidal + conical) in an FE simulation to study the hybrid arc-laser welding process of 316 steel and achieved an accurate weld cross-sectional geometry. Kong et al. [22] simulated the hybrid arc-laser welding process of mild steel with two separate volumetric heat source models (double ellipsoidal and cylindrical) and found that the fusion zone and heat-affected zone (HAZ) obtained with the FE model and experimental measurement were in good agreement. However, in their models many characteristic parameters were needed to define the heat source. Furthermore, in AM the energy produced by the heat source (arc or laser) is transferred from the top surface to the bottom of the deposited material or workpiece. Therefore, physically a surface heat source model is more representative to describe the laser or arc energy. Moreover, the characteristic parameters needed for a circular surface heat source model is only the diameter, which can be obtained readily by experiments (e.g., calorimetry for electric arc [23]). Therefore, two independent surface heat source mod-

**Table 1**
Fixed parameters used during the experiments.

| Parameters (unit) | Value |
|---|---|
| Copper nozzle diameter (mm) | 3.9 |
| Electrode diameter (mm) | 4 |
| Angle of electrode tip (°) | 40 |
| Set-back of electrode (mm) | 2.4 |
| Nozzle to plate stand-off (mm) | 8 |
| Plasma gas flowrate (L/min) | 0.8 |
| Shielding gas flowrate (L/min) | 8 |
| Oxygen level in enclosure (ppm) | <500 |
| Angle of plasma torch (°) | 20 |
| Angle of laser head (°) | 30 |
| Fibre diameter of laser (µm) | 300 |

els might be more suitable to describe the laser and arc energy in hybrid arc-laser AM simulation. However, the heat convection effect associated with fluid flow inside the melt pool is not considered in a typical FE analysis with a surface heat source model, which might affect the accuracy of the results. Such a drawback could be overcome by artificially increasing the thermal conductivity in the melt pool [24,25], but the characteristics of the artificial conductivity needed are still not well known.

Here, a 3D steady-state FE model with two independent circular surface heat sources was established to study the thermal behaviour in hybrid plasma transferred arc (PTA)-laser AM of Ti-6Al-4V. The FE model was validated by experimental data, and the advantages were compared with a FE model with two independent double ellipsoidal heat sources. Also, the effect of different process parameters, including laser power, travel speed, laser beam size, and arc-laser separation distance, on the thermal behaviours (melt pool geometry, cooling rate, and thermal gradient) was investigated quantitatively.

## 2. Experimental

### 2.1. Materials and setup

Fig. 1a schematically shows the setup for the hybrid PTA-laser system. The material used was Ti-6Al-4V plate with the dimensions of 200 × 50 × 13 mm. An EMW power supply was used to produce the PTA, and the current and voltage were recorded by an arc monitor (AMV 4000). Pure argon was used for both shielding gas and plasma gas for the plasma torch. Also, a continuous wave IPG fibre laser with a maximum output power of 8 kW and a wavelength of 1070 nm was used. The laser head was inclined at an angle of 30° to prevent the back reflection, whilst the plasma torch was inclined at an angle of 20° to avoid the burning by the laser beam. The motion of the system was provided by a 6-axis Fanuc robot. The experiments were carried out in an argon-filled enclosure to avoid oxidation of the material. The oxygen level in the enclosure was monitored by an oxygen analyser. A CMOS process camera (Xiris XVC-1000) was used to monitor the melt pool. The process parameters that were kept constant during the experiments are shown in Table 1. In order to record the thermal cycles, a channel was machined at the bottom of the titanium plate, into which a type-R thermocouple was inserted. This thermocouple has a wide working temperature range (-50–1480 °C) with an accuracy of ±1.5 °C. It should be noted that the detecting tip of the thermocouple is not ideally a point but has a certain amount of area. Therefore, the temperature measured by the thermocouple is the average value within this contact area. The thermocouple was located at the mid-width of the plate and 4 mm below the top surface. A hollow plate (made of 80% silicon dioxide, 15% silicon carbide and 5% others) was used to support the titanium plate, the middle part of which was removed to ensure it has nat-
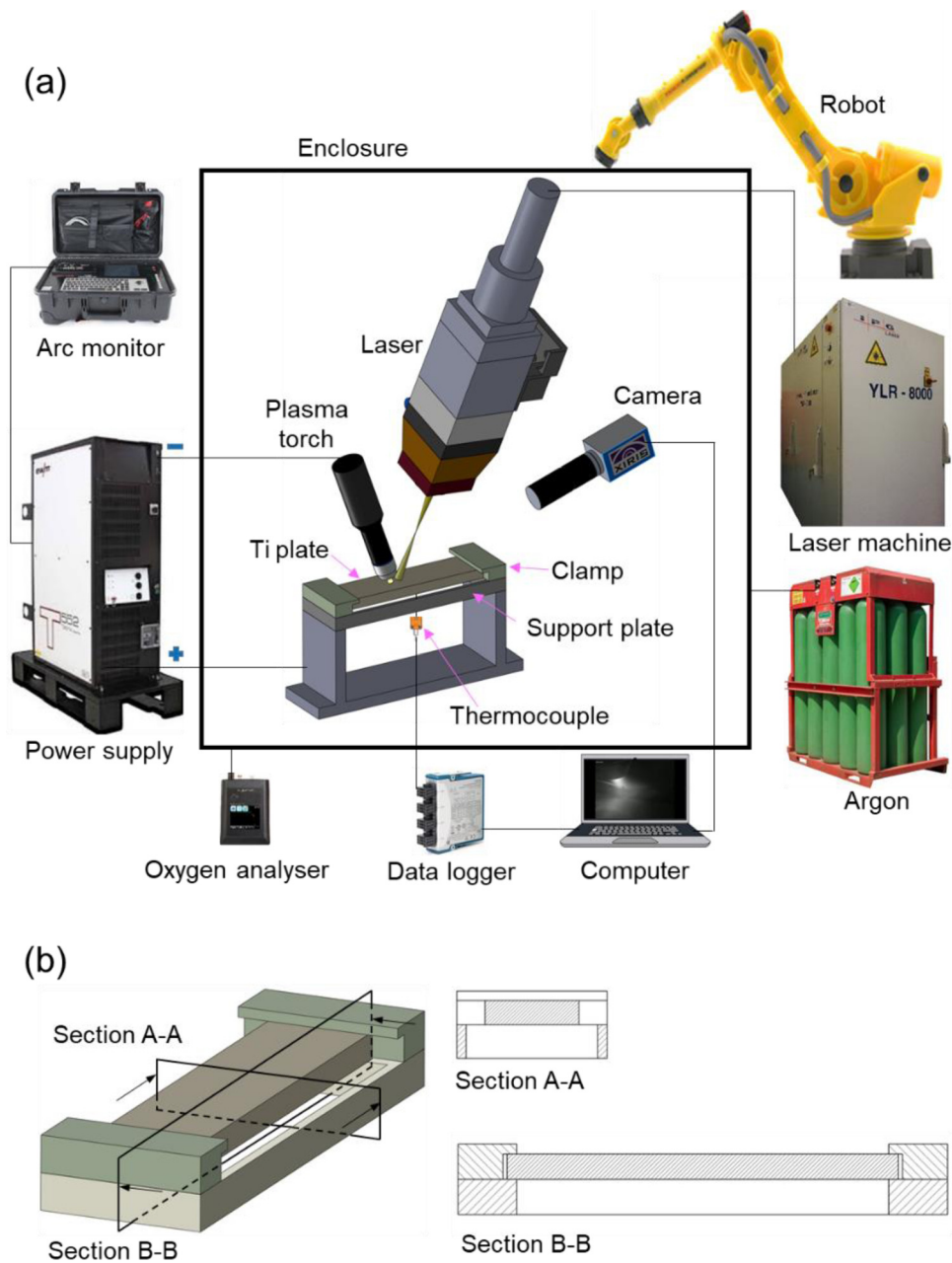
**Fig. 1.** (a) Schematic diagram showing the experimental setup for the hybrid PTA-laser system, and (b) the cross section and longitudinal section of the titanium plate, support plate and clamps.

ural heat transfer to environment and to allow the thermocouple to go through. As shown in Fig. 1b, only the two sides of the support plate were in contact with the titanium plate (5 mm in length direction on each side). The titanium plate was clamped at both sides to be fully secured.

### 2.2. Methods

To validate the FE model, a set of autogenous welds were performed at the mid-width of the plates. All the important parameters such as current, voltage, laser power, laser beam diameter (defocused), arc-laser separation distance and travel speed are shown in Table 2. In welding or AM, the weld Peclet number, ($Pe_w = vL/\alpha$, where $\alpha$, $v$, and $L$ are the thermal diffusivity, torch travel speed, and characteristic length, respectively), is a useful way of characterising the importance of heat source travel speed on the tem-

perature distribution [26,27]. For a given material and fixed heat input, a higher weld Peclet number indicates less line energy absorption by the melt pool, leading to a lower penetration depth. For example, the weld Peclet number is 9.2 for the PTA and 4.6 for the laser in Case 1, whilst it is 13.2 for the PTA and 6.6 for the laser in Case 3 (the characteristic length used for the PTA and laser was 12 mm and 6 mm, respectively). That means the penetration depth achieved in Case 3 is expected lower than that in Case 1.

In this study, the laser leading configuration was used in all the modelling cases and experiments. After welding, all samples were cross-sectioned, hot mounted, ground, polished, and etched (using Kroll's reagent) to check the dimensions of the fusion zone and the HAZ using a Nikon stereo microscope. It should be noted that the microstructure and properties in the HAZ are different from those in the base material. Normally, coarser grains are observed in the HAZ than in base material due to the higher temperature that

**Table 2**
Parameters used in the experiments for model calibration and validation.

|        | Current (A) | Voltage(V) | Laser power (W) | Travel speed (mm/s) | Separation distance (mm) | Laser beam diameter (mm) |
|--------|-------------|------------|-----------------|---------------------|--------------------------|--------------------------|
| Case 1 | 160         | 19         | 2500            | 4.5                 | 10                       | 6                        |
| Case 2 | 160         | 19         | 4500            | 4.5                 | 10                       | 6                        |
| Case 3 | 160         | 19         | 2500            | 6.5                 | 10                       | 6                        |
| Case 4 | 160         | 19         | 2500            | 4.5                 | 16                       | 6                        |

the materials undergo in the former region. In a micrographic image, due to the difference of grain size and corrosion resistance of the material in the HAZ and base material, there is a clear boundary between them after etching, which can be used to determine the HAZ boundary. In addition, some microstructure images were taken using a Hirox microscope.

## 3. Finite element modelling

### 3.1. Heat source model

A 3D steady-state FE model was developed in the present work to predict the melt pool geometry and the thermal field outside the melt pool in hybrid PTA-laser AM. Two independent circular surface heat source models with a Gaussian distribution were used for the PTA and laser. The power density distribution of the PTA or laser is described as follows:

$$q(x,y) = \frac{3Q}{\pi r_0^2} \exp\left(-3\frac{r^2}{r_0^2}\right) \tag{1}$$

where $r$ is the radial distance from a given point to the heat source centre, $r_0$ is the effective radius and defines the region where 95% of the heat flux is applied, and $Q$ is heat input. In this study, the radii of the PTA and laser used were 6 and 3 mm, respectively. For the PTA, the heat input, $Q_1$, is expressed by:

$$Q_1 = \eta_1 VI \tag{2}$$

where $V$ and $I$ are the arc voltage and arc current, respectively, and $\eta_1$ is arc efficiency. For the laser, the heat input, $Q_2$, is expressed by:

$$Q_2 = \eta_2 P \tag{3}$$

where $\eta_2$ is laser absorptivity, $P$ is the applied laser power.

Unlike a transient FE model which uses a Lagrangian reference frame to simulate the moving heat source, the steady-state model uses an Eulerian reference frame where the material "flows" through the mesh [16]. A mass flow rate per area, $F$, is utilised to represent the heat source movement, which is defined by:

$$F = -v\rho \tag{4}$$

where $\rho$ is the material density, and $v$ is the heat source travel speed.

To compare the surface heat source model with a volumetric heat source model, a 3D steady-state FE model with the commonly used double ellipsoidal heat source was also built. In this model, two independent double ellipsoidal heat sources were used for the PTA and laser. Apart from the heat source, all the settings of this FE model are the same as those in the model with surface heat sources. The power density distribution of a double ellipsoidal heat source is described as follows: [28].

$$q(x,y,z) = \frac{6\sqrt{3}Qf_f}{abc_f\pi\sqrt{\pi}} \exp\left(-\frac{3x^2}{c_f^2} - \frac{3y^2}{a^2} - \frac{3z^2}{b^2}\right) \tag{5}$$

$$q(x,y,z) = \frac{6\sqrt{3}Qf_r}{abc_r\pi\sqrt{\pi}} \exp\left(-\frac{3x^2}{c_r^2} - \frac{3y^2}{a^2} - \frac{3z^2}{b^2}\right) \tag{6}$$

**Table 3**
Thermo-physical properties of Ti-6Al-4V and other physical constants.

| Parameters (unit) | Value |
|-------------------|-------|
| Liquidus temperature (K) | 1928 [30] |
| Solidus temperature (K) | 1878 [30] |
| $\beta$-transus temperature (K) | 1270 [11] |
| Heat convection coefficient (W m$^{-2}$ K$^{-1}$) | 15 |
| Radiation emissivity | 0.4 |
| Stefan-Boltzmann constant (W m$^{-2}$ K$^{-4}$) | $5.67 \times 10^{-8}$ |
| Specific heat (J kg$^{-1}$ K$^{-1}$) | Temperature-dependent [29] |
| Density (kg m$^{-3}$) | Temperature-dependent [29] |
| Thermal conductivity (W m$^{-1}$ K$^{-1}$) | Temperature-dependent [29] |

where $a$ and $b$ are the semi-axes of the ellipsoid in the directions $y$ and $z$, respectively; $c_f$ and $c_r$ are the semi-axes of the front and rear ellipsoids in the direction $x$, respectively, and $f_f$ and $f_r$ are the fractions of heat deposited on the front and rear ellipsoids of the model, respectively, which satisfy that $f_f + f_r = 2$. It should be mentioned that artificial conductivity was not used in this model.

### 3.2. Boundary and initial conditions

Both convection and radiation were considered on the external surfaces of the plate to simulate the heat loss to the environment, which is defined by:

$$k(\nabla T \cdot n) - q + h(T - T_0) + \varepsilon\sigma\left(T^4 - T_0^4\right) = 0 \tag{7}$$

where $k$ is the thermal conductivity, $n$ is the unit outward normal vector, $q$ is the heat flux received by the surface (only top surface in this case), $h$ is the convection coefficient, $\varepsilon$ is the emissivity coefficient, $\sigma$ is the Stefan-Boltzmann constant ($5.67 \times 10^{-8}$ W m$^{-2}$ K$^{-4}$), and $T_0$ is the ambient temperature. The convection coefficient and emissivity are dependent on many factors, such as material properties and temperature. The sensitivity analysis of the convection coefficient and emissivity showed that the heat loss due to surface convection and radiation are very low compared to the heat input provided by the heat sources, meaning that the results are not sensitive to these two parameters. Therefore, constant values were used for these two parameters. The convection coefficient and emissivity were adjusted until the simulated and measured thermal fields are in good agreement. The calibrated values for convection coefficient and emissivity were 15 W m$^{-2}$ K$^{-1}$ and 0.4, respectively. The ambient and initial temperatures were set as 20 °C.

### 3.3. Material properties

The material used in this study was Ti-6Al-4V. The temperature-dependent material properties, including specific heat, density, and thermal conductivity, were taken from Ref. [29]. The thermo-physical properties of Ti-6Al-4V and other physical constants employed in the model are listed in Table 3. Artificial thermal conductivity was used in the melt pool to compensate for the convection effect associated with liquid metal motion and thus to calibrate the model. Specifically, an orthotropic conductivity ($k_x$, $k_y$, $k_z$) was used for the calibration of the model,
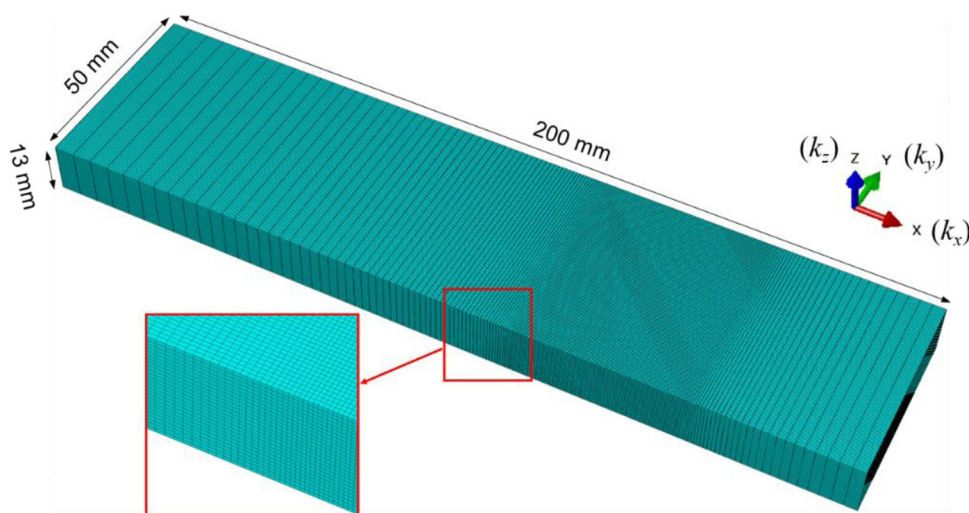
**Fig. 2.** Geometry and mesh used in the FE model.

where $k_x$, $k_y$, and $k_z$ represent the component of the thermal conductivity in $x$, $y$, and $z$ direction, respectively (indicated in Fig. 2). These parameters are determined by experimental calibration, which will be presented in Section 4.1.1. It should be mentioned that in the proposed model, the energy in the melt pool is transferred to the solid material through artificial conductivity, which is calibrated against experimental results. In this way, the power density distribution effect under inclined arc and laser can be taken into account during the calibration of artificial conductivity.

### 3.4. Numerical implementation

The model was developed using the commercial FE software ABAQUS. User-defined subroutine, DFLUX, in Fortran language was used to define the heat source. The dimensions of the titanium plate in the model were the same as those used in the experiments. The computational domain was discretised using non-uniform hexahedral meshes with an 8-node convection/diffusion brick element type (DCC3D8), as shown in Fig. 2. Due to the high temperature gradient in the heat source zone, a higher mesh density was used (grid size of 0.5 mm) in this area. In addition, to improve the computing efficiency, the mesh was set coarser at a further distance from the heat source, with a grid size of 3 and 5 mm at the two sides of the plate, respectively. Galerkin method was used to construct the discretised governing equation based on the heat transfer theory. Newton-Raphson method was employed to solve the nonlinear governing equation iteratively.

A mesh independence analysis was undertaken to assess the sensitivity of the predicted results to mesh size and to determine a reasonable mesh density. Four different mesh arrangements, consisting of 130,000, 439,400, 765,426, and 1,002,972 elements, respectively, were used for this study. Fig. 3 shows the width and depth of the melt pool obtained with four different mesh sizes. One can see that the mesh density has a very minor effect on the melt pool dimensions except that a very slight increase in the melt pool width (from 11.95 to 12.24 mm) occurred when the element number was increased from 130,000 to 439,400. Therefore, in this study, a total element number of 439,400 was selected for all the FE modelling cases. It took 3 min and 15 s for the calculation of Case 1 using a high-performance computer with $8 \times 1.6$ GHz CPU, and it took similar time for other cases using the same computational resources.
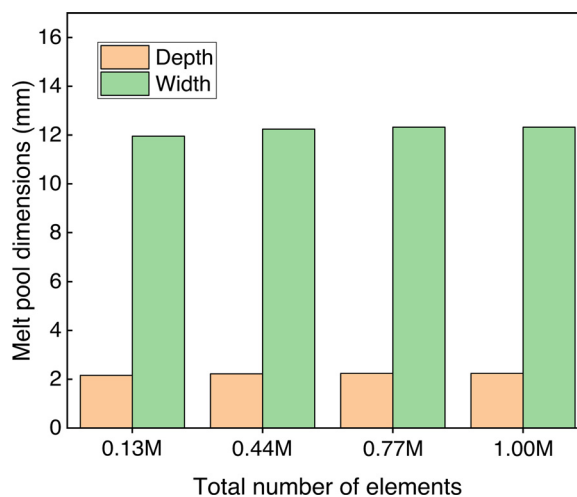


**Fig. 3.** Predicted melt pool dimensions obtained with four different mesh sizes, see process parameters for Case 1 of Table 2.

## 4. Results and discussion

### 4.1. Model calibration

#### 4.1.1. Surface heat source model

The process parameters in Case 1 (see Table 2) were used for the calibration of the FE model with two circular surface heat sources. It was found that the heat input primarily determines the melt pool volume as well as the thermal cycles. Since the arc current, arc voltage, and applied laser power were known from the experiments, the only parameters determining the heat input are arc efficiency and laser absorptivity. In fact, the laser absorptivity and arc efficiency are affected by many factors, such as temperature and melt pool surface deformations [31–33]. However, it is very difficult to capture an accurate value in additive manufacturing conditions. For example, the laser absorptivity could have a nonuniform distribution on the melt pool surface due to the different curvature. Therefore, fixed values were used in this model to represent the overall effect of this parameter, and similar approach has also been used by other researchers [34–36]. The laser absorptivity and arc efficiency were determined by experimental calibration. During calibration, different values of the aforemen-
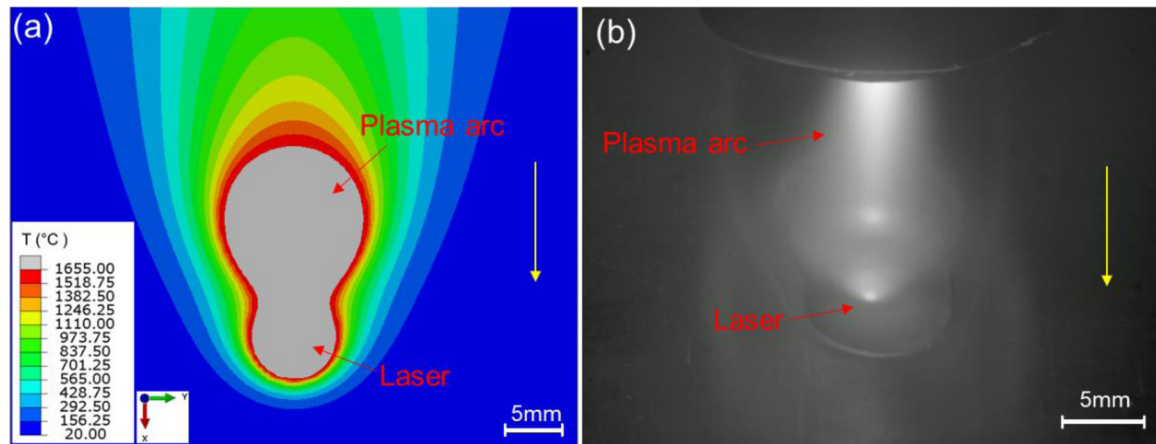
**Fig. 4.** The melt pool obtained with (a) FE model, and (b) experiment. All the parameters used are from Case 1 in Table 2. The yellow arrows indicate the heat source travel direction.

**Table 4**
Artificial conductivity used for the calibration of the FE model with two circular surface heat sources.

| $k_x$ (W m$^{-1}$ K$^{-1}$) | $k_y$ (W m$^{-1}$ K$^{-1}$) | $k_z$ (W m$^{-1}$ K$^{-1}$) |
|---|---|---|
| 100 | 150 | 30 |

**Table 5**
The dimensions of melt pool and HAZ obtained with the experiment and the FE model with two circular surface heat sources.

| | Dimensions | Experiment (mm) | FE model (mm) | Error (%) |
|---|---|---|---|---|
| Melt pool | Width | 11.4 | 12.2 | 7.0 |
| | Depth | 2.0 | 2.2 | 10.0 |
| | Length | 20.3 | 20.4 | 0.5 |
| HAZ | Width | 18.1 | 17.8 | 1.7 |
| | Depth | 7.0 | 7.3 | 4.3 |

tioned two parameters were used to compare the simulated and experimental results, including thermal history, fusion boundary, and HAZ boundary. The laser absorptivity and arc efficiency were obtained until the simulated and experimental results are in good agreement. The calibrated arc efficiency was 0.64, which is consistent with the measurement by Fuerschbach and Knorovsky [37], ranging from 0.5–0.75. The calibrated laser absorptivity was 0.5, which also agrees with the values of a fibre laser in conduction mode for titanium, ranging from 0.38–0.51 [38–41].

Orthotropic artificial conductivity above liquidus temperature was then used to calibrate the melt pool geometry. More specifically, the melt pool size in one certain direction can be increased by increasing the conductivity in this direction, which then is compensated by the melt pool size in the remaining dimensions. The conductivities used in x, y and z directions are shown in Table 4. The artificial conductivities used in x and y directions are much larger than that in z direction. Actually, in the conduction mode of welding or AM, heat convection dominates the heat transfer in the melt pool [42]. The fluid flow produced by the plasma arc is mainly controlled by the surface forces, such as Marangoni shear stress, arc pressure, and arc shear stress [43]. Similarly, the fluid flow induced by the laser in conduction mode is dominated by the Marangoni shear stress, which is also surface force [44]. In addition, the fluid flow direction is also influenced by material composition [45,46]. In this study, Ti-6Al-4V was used with a negative temperature-dependent surface tension coefficient, which can cause strong sideward and backward surface flows [43]. Therefore, the heat convection in width and length directions are much larger than that in depth direction. In the proposed model, as the artificial conductivity is applied in the melt pool to compensate for the heat convection effect, therefore the calibrated artificial conductivities in x and y directions are significantly larger than that in z direction.

Fig. 4 shows the melt pool obtained with the FE model and experiment. It can be seen from both simulation and experiment that the laser produced a much smaller melt pool compared to the PTA, but the two melt pools were connected and formed one elongated melt pool.

Fig. 5 shows the comparison of the melt pool, HAZ, and thermal cycle between the FE model and experiment, and Table 5 shows the dimensions of the corresponding melt pool and HAZ. For Ti-6Al-4V, the fusion line at cross-section is difficult to identify due to the smooth transition of microstructure. Many researchers reported that it is close to the interface between columnar and equiaxed grains [24,43,47,48], and therefore a red dashed line was drawn to indicate the fusion line (Fig. 5a), which can be used to identify the depth of the melt pool. The width of the melt pool can be identified easily by visual check from the top surface of the plate. As the HAZ boundary is easy to identify, it was also compared to ensure a more accurate result. All the positions in the cross-section do not reach a peak temperature at the same time, meaning that the deepest points of the HAZ boundary and fusion line are not located in the same cross-section in the FE model. Therefore, the comparison of HAZ is presented separately in Fig. 5b. In simulation, the HAZ can be determined by two isotherms. One is the solidus isotherm, which is the boundary of the HAZ and melt pool. The other is the $\alpha$-dissolution isotherm, which is the boundary of the HAZ and base material. The $\alpha$-dissolution temperature used in this study was 747°C, at which the $\alpha$ phase starts to dissolve into $\beta$ phase [47].

From Fig. 5a, b, and Table 5, the melt pool and HAZ from the simulation and experiment match well. Fig. 5c shows the comparison of the melt pool at the top surface, where both the shape and the dimensions show good agreement. Fig. 5d shows that the thermal cycle obtained with the FE model is in good agreement with the experimental measurement, except for the peak temperature. The slight mismatch in peak temperature arises because the simulated melt pool is slightly deeper than that in experiment (see Fig. 5a), and thus the selected position is closer to the fusion line in simulation than in experiment, leading to a slightly higher value of peak temperature in simulation. Overall, the results presented in Fig. 5 demonstrate a high validity of the FE model.
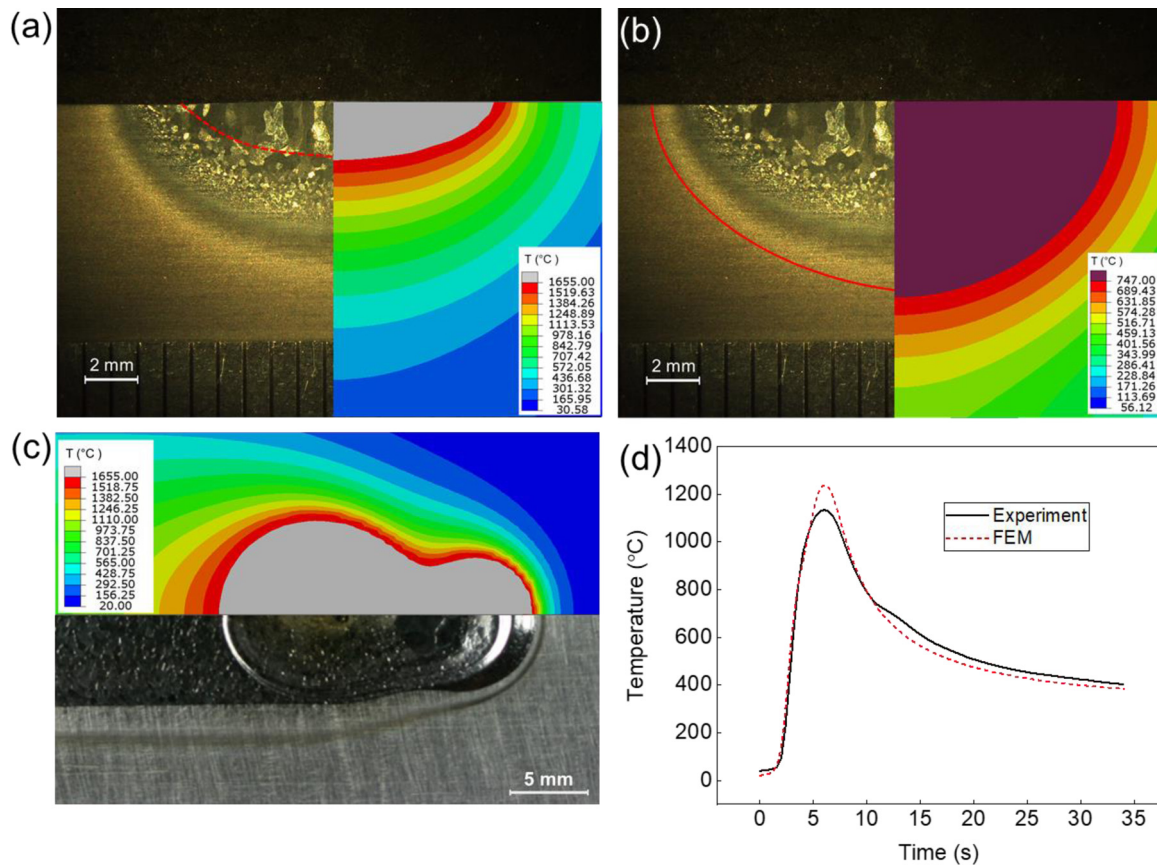
**Fig. 5.** Comparison between the FE model with two circular surface heat sources and the experimental data: (a) melt pool at cross-section, (b) HAZ at cross-section, (c) melt pool at top surface, and (d) the thermal cycle at the mid-width and 4 mm below the top surface of the plate.

**Table 6**
Calibrated parameters for the two double ellipsoidal heat sources.

| Heat source | $a$ (mm) | $b$ (mm) | $c_f$ (mm) | $c_r$ (mm) | $f_f$ | $f_r$ |
|---|---|---|---|---|---|---|
| Laser | 7 | 1 | 4 | 8 | 0.6 | 1.4 |
| PTA | 14 | 1 | 6 | 12 | 0.6 | 1.4 |

**Table 7**
The dimensions of melt pool and HAZ obtained from the experiment and the FE model with two double ellipsoidal heat sources.

| Dimensions | | Experiment (mm) | FE model (mm) | Error (%) |
|---|---|---|---|---|
| Melt pool | Width | 11.4 | 11.4 | 0 |
| | Depth | 2.0 | 2.2 | 10.0 |
| | Length | 20.3 | 20.0 | 1.5 |
| HAZ | Width | 18.1 | 22.0 | 21.5 |
| | Depth | 7.0 | 7.5 | 7.1 |

### 4.1.2. Volumetric heat source model

The same process parameters (Case 1 in Table 2) were used for the calibration of the FE model with two double ellipsoidal heat sources. Some characteristic parameters for the heat sources (i.e., PTA and laser) need to be adjusted for the calibration of this model, which are shown in Table 6. In addition, an isotropic thermal conductivity of 30 W m$^{-1}$ K$^{-1}$ was used above the liquidus temperature. The same arc efficiency and laser absorptivity (0.64 and 0.5, respectively) were used as those in the FE model with surface heat sources as described in Section 4.1.1. Fig. 6 and Table 7 show the comparison of the melt pool, HAZ, and thermal cycle between the FE model and experiment. Both the melt pool geometry and the thermal cycle match well. However, the HAZ obtained

from this model is relatively large compared to that from the experimental measurement (e.g., 21.5% larger in width), which will be discussed in the next section.

### 4.2. Advantages of the surface heat source model

For the calibration of both surface and volumetric heat source models, several parameters are needed to define the heat sources, which are schematically shown in Fig. 7. For the circular surface heat source model, the only geometric parameter needed is the diameter of the heat source ($r$), which can be obtained by experimental measurement (e.g., electric arc) or equipment setting (e.g., laser). Therefore, for the calibration of the FE model with two circular surface heat sources, the only empirical parameters that need to be adjusted are the conductivity in three orthogonal directions (i.e., $k_x$, $k_y$, and $k_z$), as demonstrated in Table 4. However, for the calibration of a double ellipsoidal heat source model, four geometric parameters need to be adjusted for the PTA or laser, meaning that eight geometric parameters to be determined for the hybrid PTA-laser AM process. In addition, the fractions of heat deposited on the front and rear part of the model (i.e., $f_f$ and $f_r$) are also adjustable [28]. It can be seen from Table 6 that twelve parameters were calibrated for the two double ellipsoidal heat sources. Furthermore, sometimes an isotropic artificial conductivity is also used in the melt pool to achieve more realistic temperatures in the melt pool [16,49], increasing the complexity of the calibration work. Therefore, for the calibration of the FE model with two double ellipsoidal heat sources, the number of the parameters that need to be adjusted is twelve or thirteen. This is much more than that of the FE model with two circular surface heat sources (only
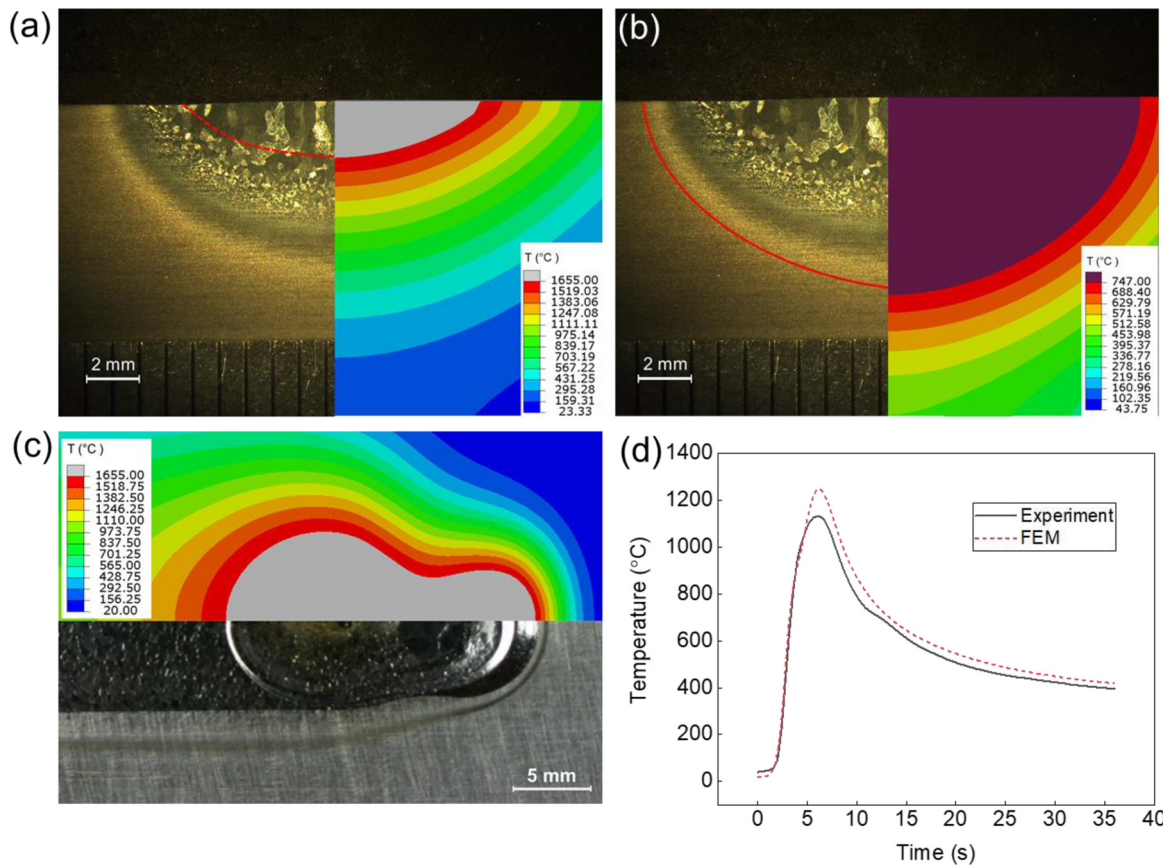
**Fig. 6.** Comparison between the FE model with two double ellipsoidal heat sources and experimental results: (a) melt pool at cross-section, (b) HAZ at cross-section, (c) melt pool at top surface, and (d) the thermal cycle at the mid-width and 4 mm below the top surface of the plate.
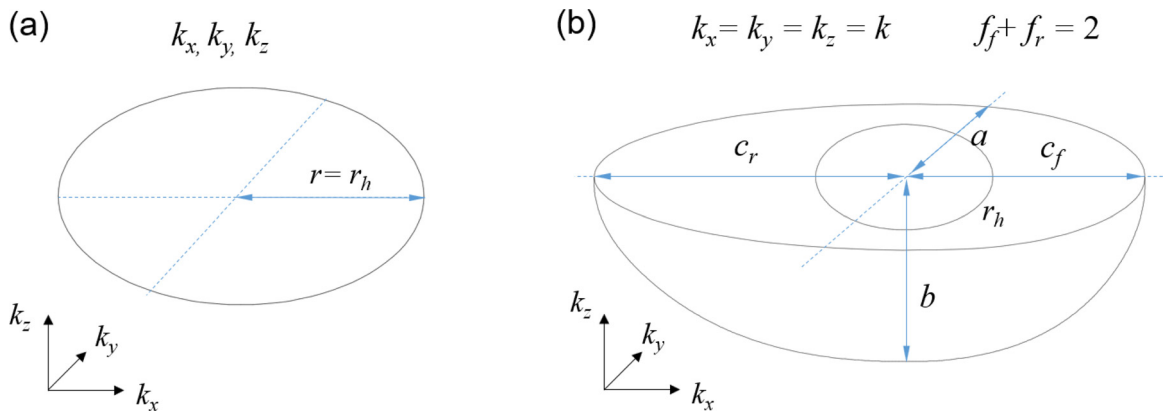


**Fig. 7.** Comparison of the parameters needed for the calibration of the FE models with (a) a circular surface heat source, and (b) a double ellipsoidal heat source. $r_h$ is the actual radius of a heat source (e.g., PTA and laser).

three), meaning that the calibration is much simpler for the surface heat source model.

As discussed earlier, the only geometric parameter needed for a circular surface heat source model is the radius ($r$), which can be obtained from experiments ($r_h$). This means that the heat source size used in the surface heat source model is clearly defined by the process, as illustrated in Fig. 7a. However, for a double ellipsoidal heat source model, the geometric parameters that determine the heat source size need to be adjusted for calibration purpose. This means the heat source size is an empirical parameter, which cannot be directly obtained from the process. In this study, for example, after calibration the double ellipsoidal heat source sizes required for both the laser and the PTA in the FE model are much

bigger than those used in actual process (see Fig. 7b). For example, a width of 14 mm and a length of 12 mm were used for the laser, whilst a diameter of 6 mm was used in experiment. Similarly, a much larger PTA size was used in the double ellipsoidal heat source model than in experiment. Since the double ellipsoidal heat source does not represent the real heat source size, it is unable to study the effect of the heat source size on the hybrid process.

Some other cases (Cases 2–4 in Table 2) were also simulated to demonstrate the general applicability of the calibration and to compare the prediction accuracy between the surface and volumetric heat source models. For the circular surface heat source model, the same artificial conductivity that was used in Case 1
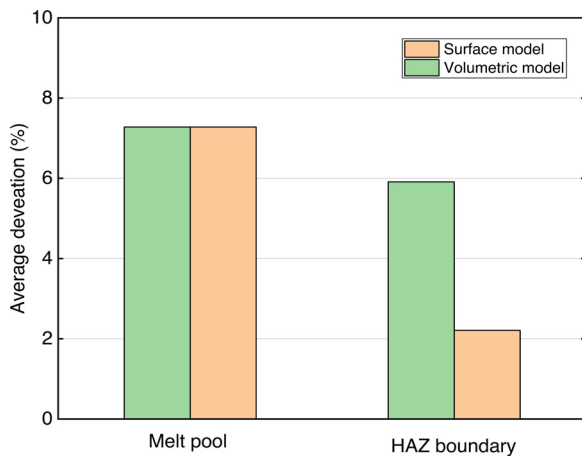
**Fig. 8.** Prediction accuracy for Cases 2–4 with the surface and volumetric heat source models.

was used for Cases 2–4. Similarly, for the double ellipsoidal heat source model, the same empirical parameters that were used in Case 1 were adopted for Cases 2–4. This means that both models have been calibrated only once. Different deviations in melt pool dimensions between experiments and FE models were observed. As shown in Fig. 8, for the surface heat source model, the average deviation was 7.28% for melt pool (including width, depth, and length) and 2.21% for HAZ (including width and depth), demonstrating a good applicability of the calibration. For the volumetric heat source model, a same average value of 7.28% was achieved for melt pool, but an average value of 5.91% was achieved for the HAZ.

Compared to the surface heat source model, the relatively high prediction errors in HAZ in the volumetric h3eat source model is mainly attributed to the mismatch of HAZ during calibration as described in Section 4.1.2. Fig. 9 shows the scenario that the HAZ dimensions are matched well during calibration (Fig. 9a), where, however, there is a significant difference in the melt pool dimensions between the FE model and experiments (Fig. 9b and c). This means that an accurate calibration on both melt pool and HAZ cannot be achieved using two double ellipsoidal heat sources. On the one hand, this is because during the calibration of the volumetric heat source model, the heat source size selected might not be based on the experimental measurement. For example, in this study, the heat source size used is much larger than the actual one and even larger than the melt pool width. This means that a proportion of energy is applied on the HAZ, leading to an inaccurate HAZ geometry. On the other hand, if the actual heat source size is used for the volumetric heat source model, an accurate melt pool geometry then could not be achieved. This is because there is limitation of combining two double ellipsoidal heat sources for simulating the heat transfer in the hybrid process. As schematically shown in Fig. 10, in practice the heat will transfer from the top surface to the bottom of the workpiece, meaning that physically two surface heat sources are representative for the heat transfer in the hybrid process (Fig. 10a). However, with two volumetric heat sources the heat transfer in the material is unrepresentative and this becomes worse in the middle area of the two heat sources due to their interaction (highlighted by the dashed blue box in Fig. 10b). This means that the heat transfer obtained with the two double ellipsoidal heat sources cannot represent the real situation, leading to an inaccurate geometry on melt pool and HAZ.

Fig. 11 shows the comparison of the melt pool obtained with the process parameters in Case 4. Although the melt pool dimensions obtained with both surface and volumetric heat source models have good agreement with experimental measurement, there is a

difference in melt pool geometry. Fig. 11a shows that the melt pool geometry obtained with the surface heat source model matches well with experiments. Fig. 11b, however, shows that the front part of the PTA-induced melt pool obtained with the volumetric heat source model has a big difference with experimental measurement (as highlighted by the yellow box). This provides more evidence showing that the FE model using two circular surface heat sources is more representative for thermal behaviour analysis for the hybrid AM process.

In fact, it is suitable and popular to use a volumetric heat source model for melt pool prediction in AM or welding processes with a single heat source, and accurate results were obtained by many researchers [13,14,28,50,51]. However, when there are two independent heat sources needed in a process like hybrid PTA-laser AM, simply combining two volumetric heat sources suffers inherent limitation to capture the complicated heating effect. This is because the combination of two volumetric heat sources could not represent the real heat transfer in the melt pool, meaning that the mathematical formulation for the model is not appropriate for the simulation of the hybrid process. An alternative way of using a volumetric heat source model for the hybrid AM process is to design a customised heat source model based on the polynomial curve fit of the experimental fusion line [52]. However, this means that a new heat source model is needed when the fusion line is changed due to different process condition used. Overall, the model developed in this study provides an efficient and representative way for the prediction of the thermal behaviour in the hybrid PTA arc-laser AM process.

### 4.3. Effect of process parameters on melt pool geometry

In metal AM, the melt pool shape is one of the primary features as it determines the geometry of the deposited bead, which is a fundamental building block for the built parts [7]. Amongst the three dimensions (width, depth, and length) of the melt pool, the width and depth are paid more attention here as they determine the printing resolution and the remelting into the underlying layers or baseplate.

Fig. 12 shows the melt pool dimensions as a function of the applied laser power. One can see that both the melt pool width and depth increase proportionally with the laser power due to the increased energy input. Fig. 13 shows the corresponding melt pool geometries in some cases presented in Fig. 12. When the laser power was at a relatively low value of 500 W, the laser could not generate a melt pool, but just preheated the workpiece. As the laser power increased to 1500 W, two separate melt pools were generated by the PTA and laser, respectively. With the further increase of laser power from 2500 to 5500 W, the two separate melt pools merged into one deeper and wider melt pool. As seen in Fig. 13, the width and depth of the melt pool are determined by the back part, which is formed by the PTA. Here, although the applied arc power is constant (3040 W), the laser adds energy in front of the PTA, and therefore the PTA-induced melt pool is enlarged with the increase of laser power.

Fig. 14 shows the effect of travel speed on the melt pool dimensions. Both the melt pool width and depth reduce with the increase of travel speed. Amongst them, the melt pool width decreases by 33.6% (from 14.3 to 9.5 mm) whilst the depth decreases by 46.4% (from 2.8 to 1.5 mm) as the travel speed increases from 2.5 to 11 mm/s. This is attributed to the decreased energy input per unit length (also referred to as line energy, $\Lambda$), which is inversely proportional to the travel speed, as given by:

$$\Lambda = \frac{Q_1 + Q_2}{v} \tag{8}$$

Therefore, the increase of travel speed at a constant input power results in a decrease in line energy, leading to a smaller
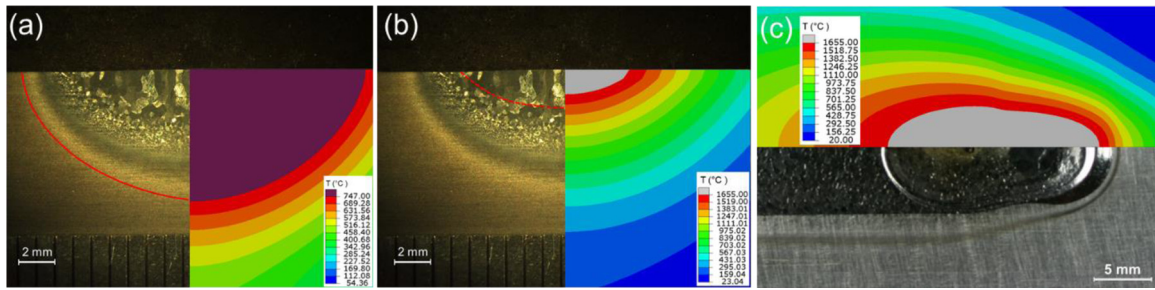
**Fig. 9.** Comparison of the melt pool geometry when HAZ is well matched: (a) well matched HAZ, (b) melt pool comparison in cross-section, and (c) melt pool comparison from top view.
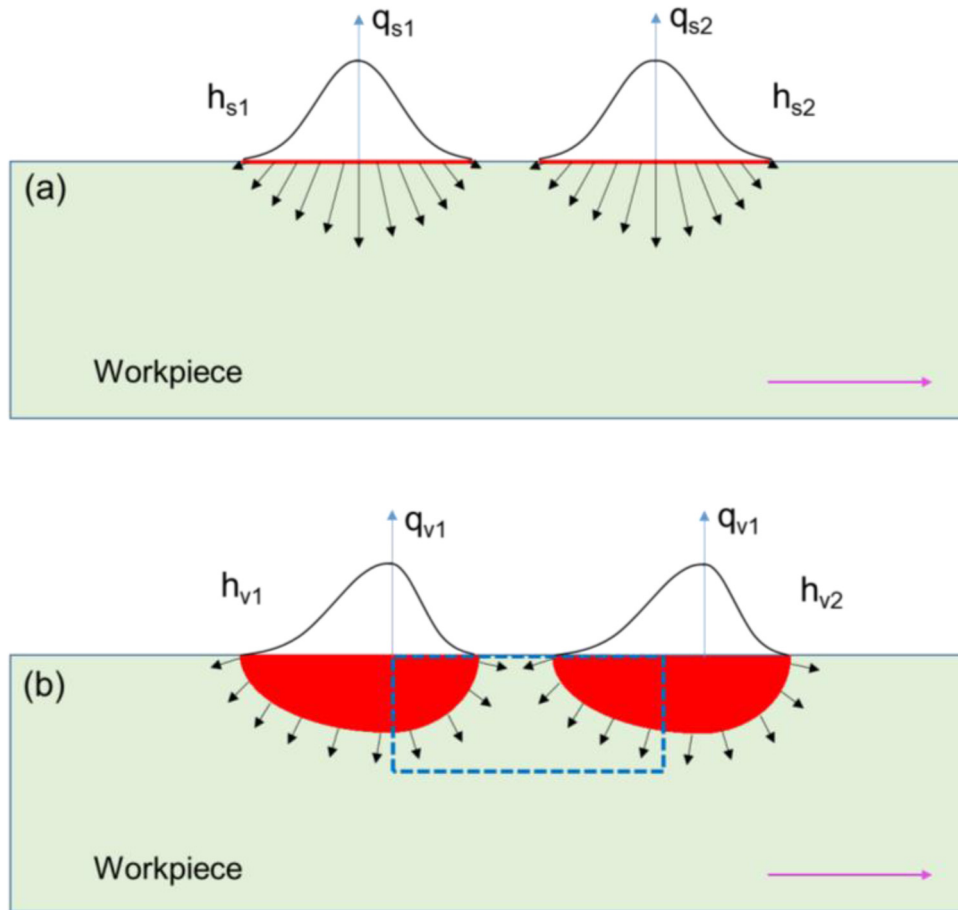


**Fig. 10.** Schematic showing the heat transfer in a workpiece with different heat source models: (a) two surface heat sources, and (b) two volumetric heat sources. Pink arrows indicate the heat source travel direction; $h_s$ and $h_v$ stand for surface heat source and volumetric heat source, respectively; $q_s$ and $q_v$ stand for the heat flux for surface and volumetric heat sources, respectively.
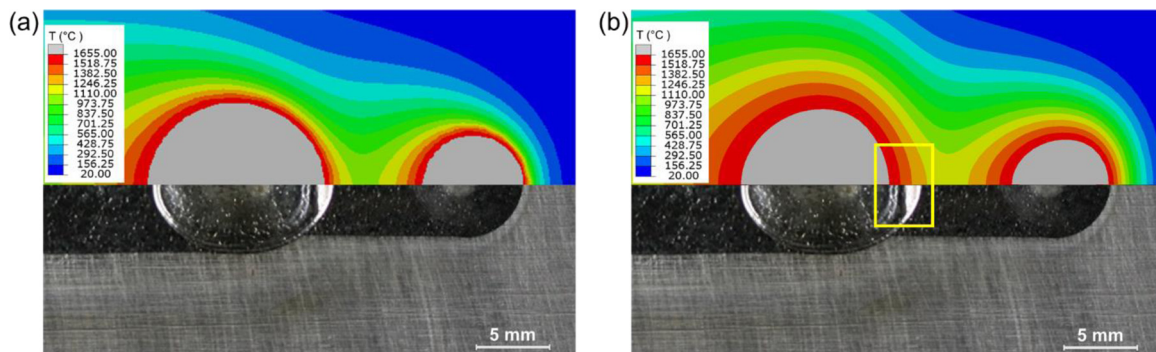


**Fig. 11.** Comparison of the melt pool prediction using two different heat source models (Case 4 in Table 2): (a) surface heat source model, and (b) volumetric heat source model.
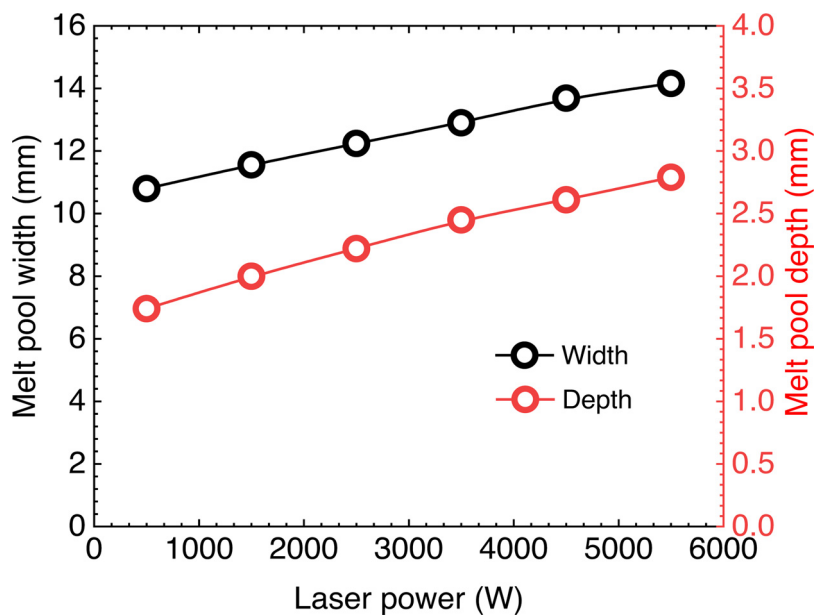
**Fig. 12.** The effect of laser power on the melt pool dimensions (all the process parameters used except laser power are the same as those in Case 1 in Table 2).
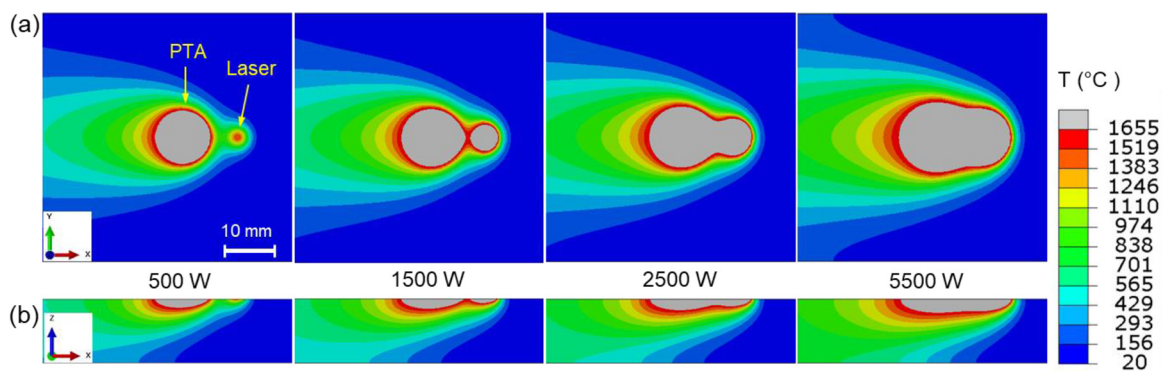


**Fig. 13.** The effect of laser power on the melt pool geometry from different views: (a) top surface, and (b) longitudinal section.
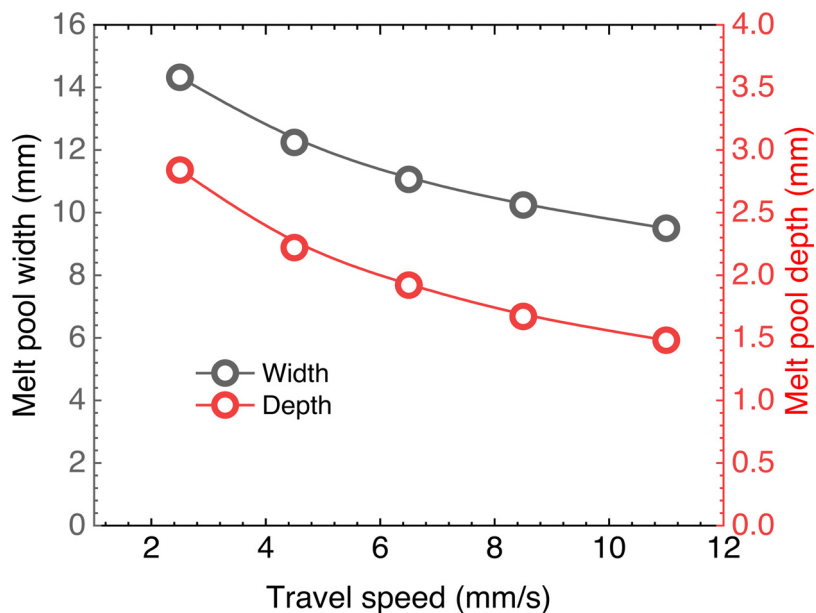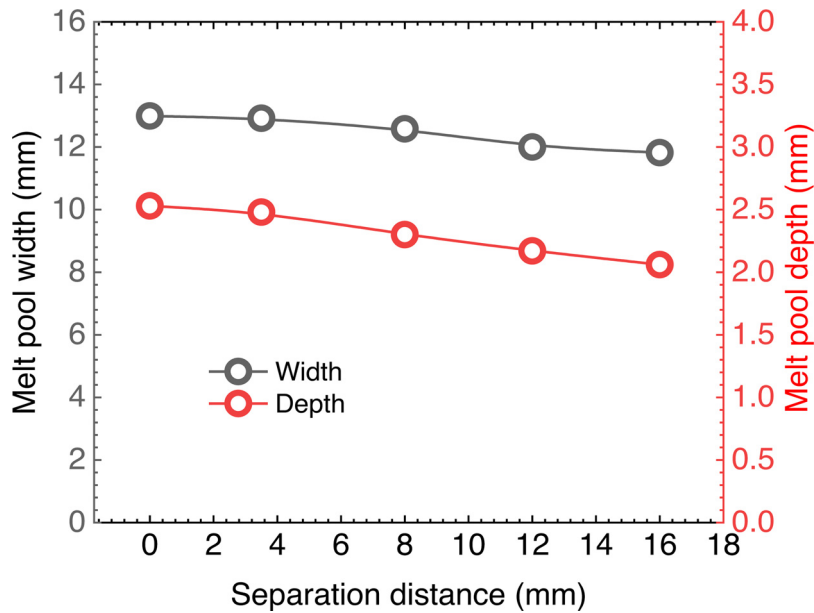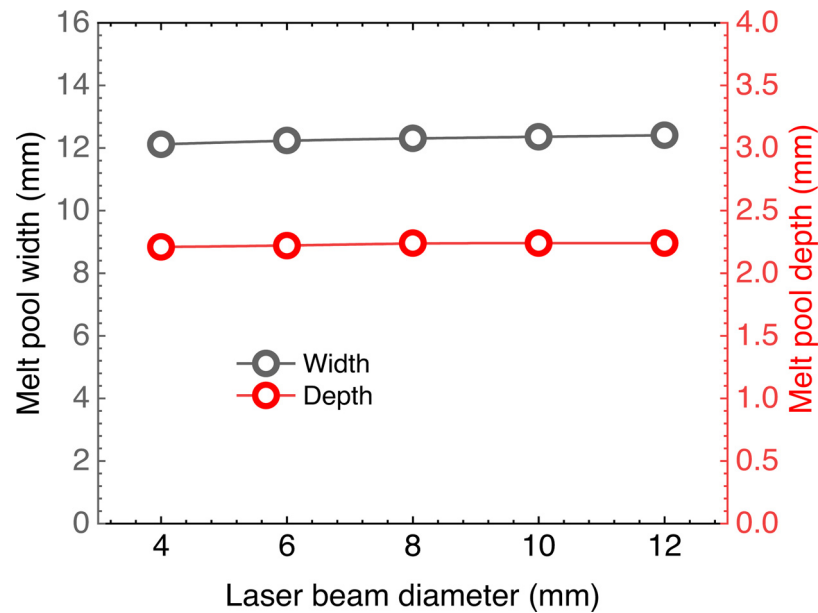


**Fig. 14.** The effect of travel speed on the melt pool dimensions (all the process parameters used except travel speed are the same as those in Case 1 in Table 2).
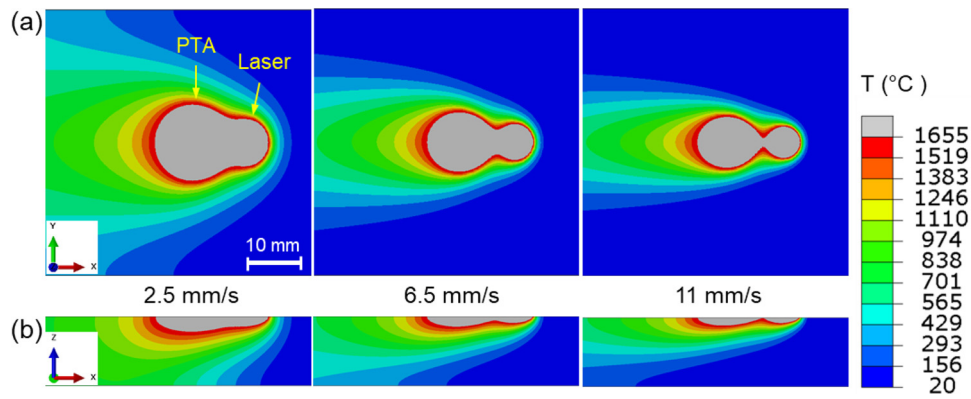
**Fig. 15.** The effect of travel speed on the melt pool geometry from different views: (a) top surface, and (b) longitudinal section.



**Fig. 16.** The effect of the arc-laser separation distance on the melt pool dimensions (all the process parameters used except separation distance are the same as those in Case 1 in Table 2).
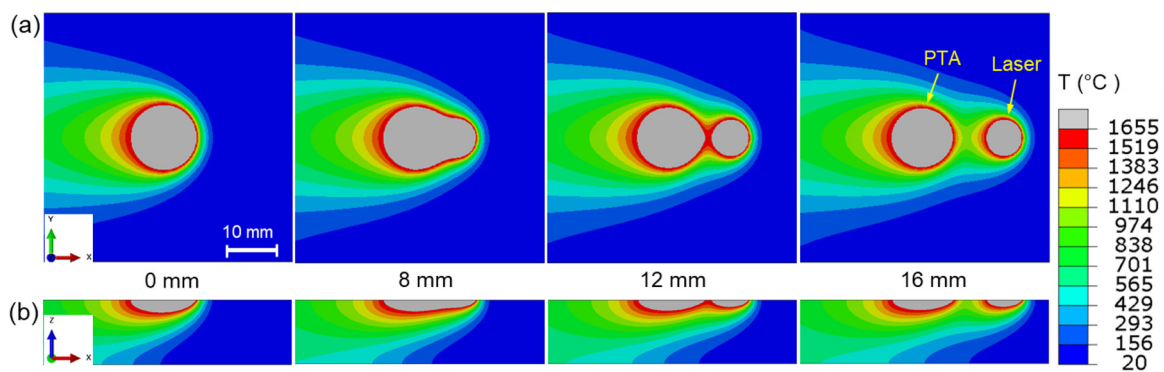


**Fig. 17.** The effect of arc-laser separation distance on the melt pool geometry from different views: (a) top view, and (b) longitudinal section.

melt pool. Fig. 15 shows the corresponding melt pool geometries in some cases presented in Fig. 14, where the melt pool becomes smaller with the increase of travel speed. Compared to the depth and width, the total length of the melt pool has no significant variation due to the fixed separation distance between the two heat sources (Fig. 15).

Fig. 16 shows the variation in melt pool dimensions with the arc-laser separation distance, and Fig. 17 shows the correspond-ing melt pool geometries in several selected cases. In general, the increasing separation distance leads to a slight decrease in both melt pool width and depth (Fig. 16) but a significant increase in the total melt pool length (Fig. 17). As the separation distance in-creases from 0 to 8 mm, there is one large melt pool, as seen in Fig. 17. However, two separate melt pools occur as it increases to or beyond 12 mm. In these cases, the total applied power is constant with 3040 W and 2500 W for arc source and laser

**Fig. 18.** The effect of the laser beam diameter on the melt pool dimensions (all the process parameters used except laser beam diameter are the same as those in Case 1 in Table 2).
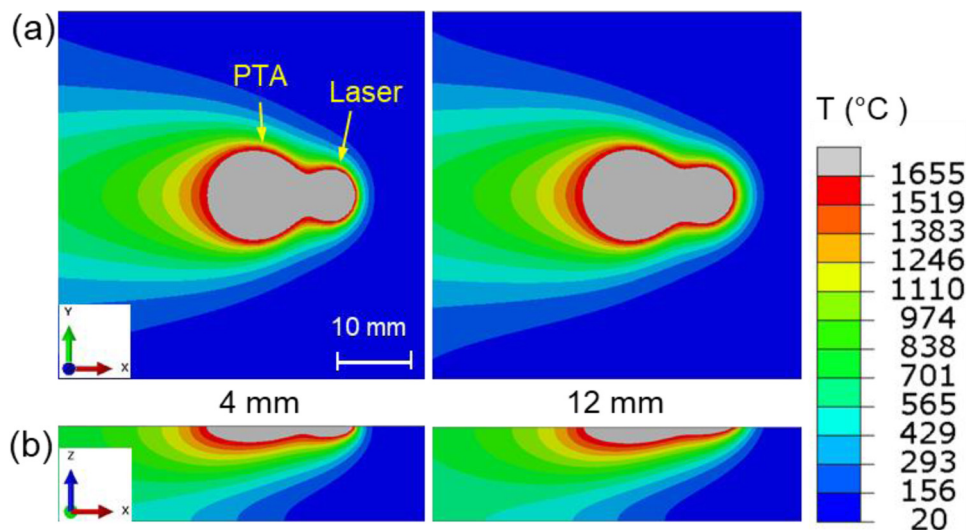


**Fig. 19.** The melt pool geometry obtained with the laser beam diameters of 4 and 12 mm from different views: (a) top view, and (b) longitudinal section.

source, respectively. The temperature in the region in front of the PTA-induced melt pool is reduced due to the increased separation distance, leading to a slight decrease in melt pool width and depth.

Fig. 18 shows the melt pool dimensions as a function of the laser beam diameter, where the laser beam size has a minor effect on both the melt pool width and depth. Fig. 19 shows the melt pool geometry produced by two extreme beam diameters of 4 and 12 mm. As seen in Fig. 19a and b, increasing the laser beam size leads to a slight increase in width and decrease in depth at the front part of the melt pool (i.e., the melt pool generated by the laser), which means the laser-induced melt pool become wider and shallower. However, this has very little effect on the rear part of the melt pool, which determines the final width and depth. This is mainly because the energy added by the laser is unchanged in all the cases, and therefore the rear part of the melt pool has not been affected. Also, the applied laser power of 2500 W is relatively low compared to the arc power of 3040 W. However, if a much higher

laser power is used with a large beam size, the laser-induced melt pool could determine the final width and depth.

In AM, the ability to achieve good surface finish of the deposited parts is of concern. Low surface waviness is desirable as it results in a low amount of material to be machined off, which is cost-effective and environmentally friendly. It is recognised that the surface finish of the deposited parts is controlled by the bead shape [7]. For the same cross-sectional area of a bead, a lower surface waviness of the deposited component can be achieved with a flatter bead shape. Although the deposited material was not considered in this FE model, it still can be used to approximate the behaviour of melt pool variation at different process parameters. From Figs. 12 and 14, we know that in hybrid PTA-laser AM the deposited beads would become wider with the increasing laser power and decreasing travel speed due to the increased energy input. Due to mass conservation, the bead height would decrease with increasing width. This is consistent with the results obtained with the hybrid PTA-laser AM experiments [10]. In addition, the
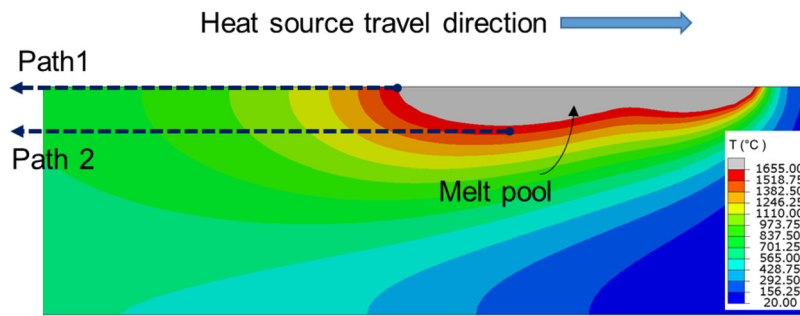
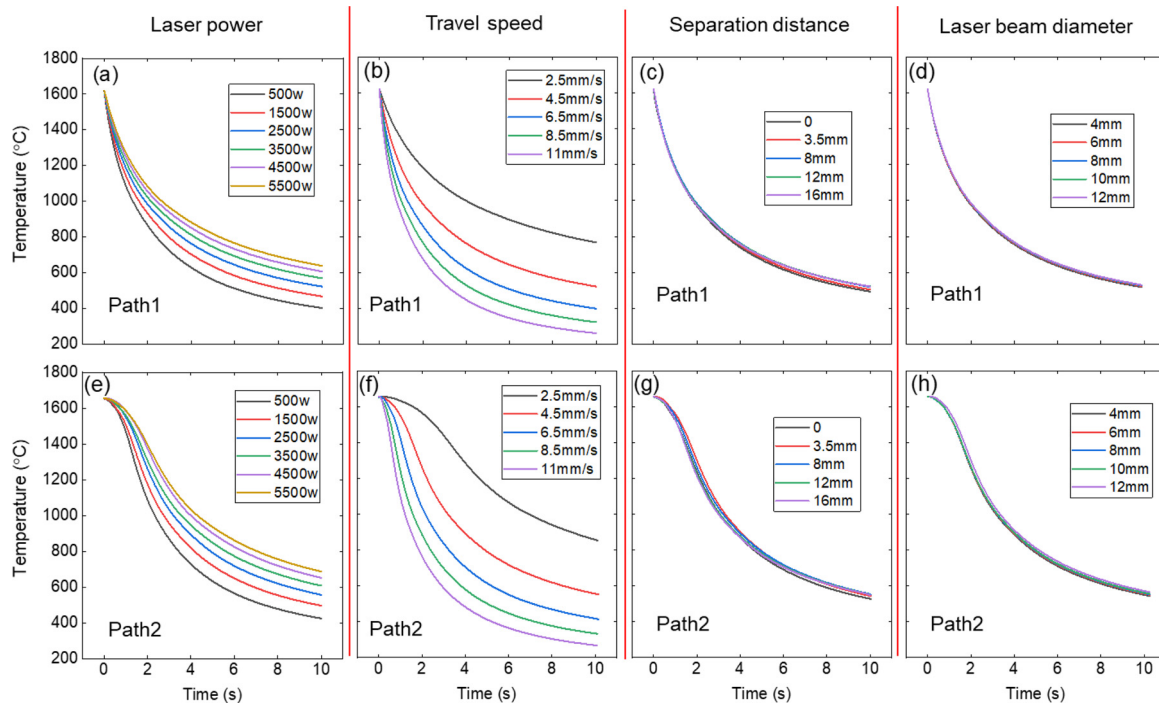**Fig. 20.** Two paths selected for the analysis of thermal conditions.



**Fig. 21.** Thermal cycles as a function of different process parameters: the effect of (a) laser power, (b) travel speed, (c) separation distance, and (d) laser beam diameter on thermal cycles along Path 1; and the effect of (e) laser power, (f) travel speed, (g) separation distance, and (h) laser beam diameter on thermal cycles along Path 2. Note, in each graph all the process parameters were kept constant except the studied one.

results about melt pool variation affected by arc-laser separation distance and laser beam diameter are also consistent with those obtained with the hybrid PTA-laser AM experiments [9,10]. These confirm that this model can be used to predict the variation trend of the bead shape for the hybrid PTA-laser AM process.

### 4.4. Effect of process parameters on thermal variables

Thermal variables such as cooling rate ($\dot{T}$) and thermal gradient ($T'$) determine the microstructure during the deposition process [11,53]. With this simplified model, the behaviour of the essential thermal variables in the hybrid AM process can be predicted which can provide useful information for metallurgical study. In this model, artificial conductivity is used in the melt pool, meaning that the temperature distribution in the melt pool might not be the same as in real conditions (this is also the limitation of an FE model which cannot capture the fluid flow in melt pool). Therefore, for the analysis of thermal variables, the temperature field above the melting point will not be discussed. As shown in Fig. 20, two paths opposite to the heat source travel direction are selected for the analysis of thermal variables, both of which are at the mid-width of the plate. Path 1 is at the top surface of the plate, and Path 2 is at the bottom of the fusion boundary.

Fig. 21 shows the thermal cycles of the positions on Path 1 and Path 2 at different process parameters. Only the cooling stage of the thermal cycles is shown here. The thermal cycle changes a lot with the variation of laser power and travel speed on both paths. More specifically, after the same period of time as the heat source passes by, a higher temperature is observed at either a higher laser power or a lower travel speed. In comparison, the separation distance and laser beam diameter have no significant effect on the thermal cycles. As mentioned earlier, this is because the variation of the latter two parameters does not change the total energy input into the workpiece, which have insignificant effect not only on melt pool geometry but also on thermal cycles. In general, laser power and travel speed are two primary process parameters affecting the thermal conditions in the hybrid PTA-laser AM process, which will be discussed in the following sections.

In addition to the temperature field, a subroutine in ABAQUS was developed to calculate the cooling rate field and thermal gradient field for the process. The cooling rate ($\dot{T}$) and thermal gradient ($T'$) are defined in Eq. (9) and Eq. (10), respectively.

$$\dot{T} = \frac{\partial T}{\partial t} \qquad (9)$$

14
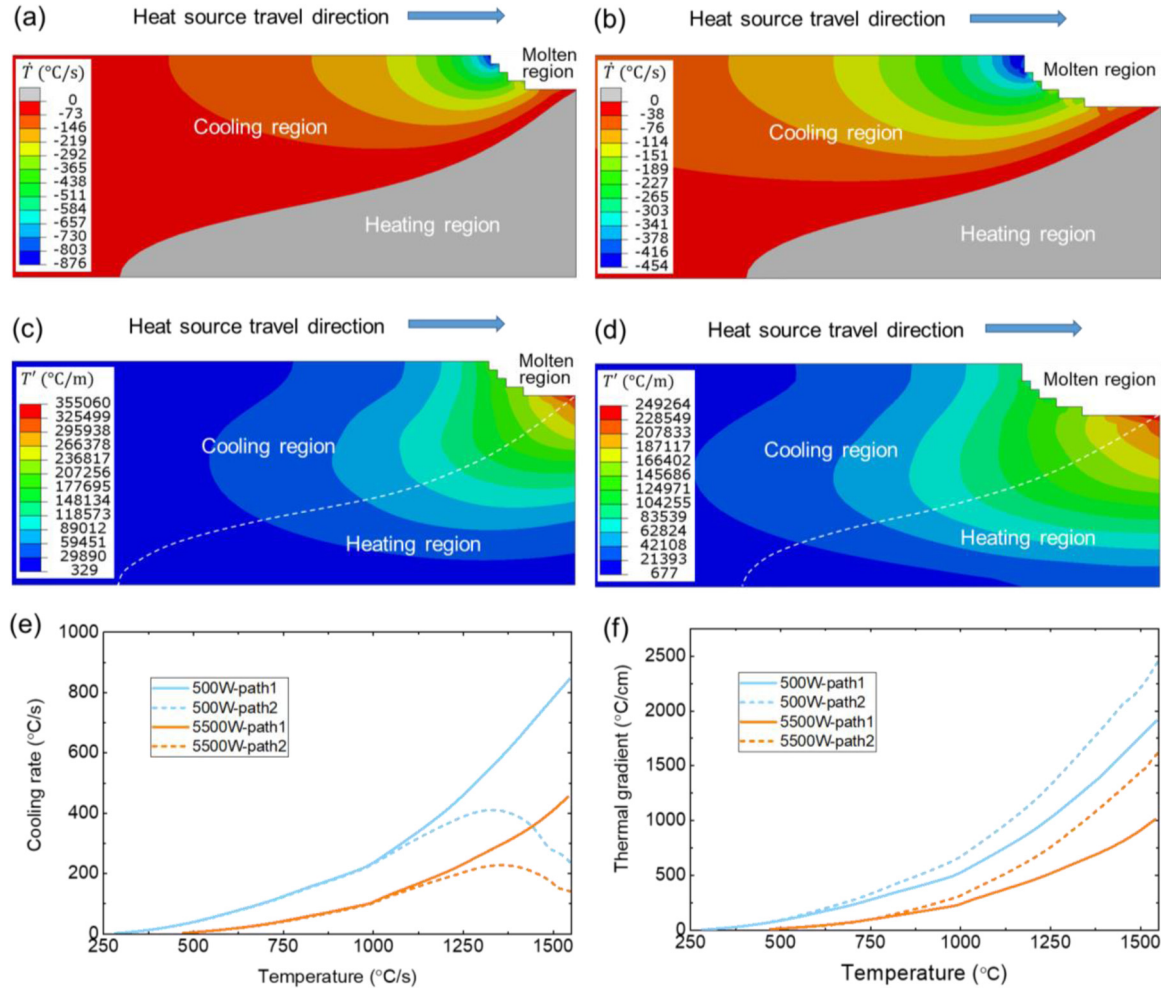
**Fig. 22.** The effect of laser power on cooling rate and thermal gradient: cooling rate contour at a laser power of (a) 500 W and (b) 5500 W; thermal gradient contour at a laser power of (c) 500 W and (d) 5500 W; the (e) cooling rate and (f) thermal gradient along Path 1 and Path 2 as a function of temperature.

$$T' = \sqrt{\left(\frac{\partial T}{\partial x}\right)^2 + \left(\frac{\partial T}{\partial y}\right)^2 + \left(\frac{\partial T}{\partial z}\right)^2} \qquad (10)$$

To circumvent the difficulty in directly calculating the 3D spatial derivatives from the discrete temperature data, an indirect approach was employed for calculation of the thermal gradient using the ABAQUS solver output. According to Fourier's law, $q_x = -k\frac{\partial T}{\partial x}$, $q_y = -k\frac{\partial T}{\partial y}$, $q_z = -k\frac{\partial T}{\partial z}$, and then $T' = \sqrt{\left(\frac{q_x}{k}\right)^2 + \left(\frac{q_y}{k}\right)^2 + \left(\frac{q_z}{k}\right)^2}$, where $q_x$, $q_y$, $q_z$ are the heat flux components in $x$, $y$, and $z$ directions, respectively, and $k$ is the thermal conductivity. A user-defined subroutine UVARM was developed to obtain the $q_x$, $q_y$, $q_z$ and $T$ from the ABAQUS solver and calculate the $T'$ accordingly. In the subroutine, the ABAQUS utility routine GETVRM was called to access to the heat flux and temperature values computed by the ABAQUS solver, which employed the linear interpolation function for the 8-node DCC3D8 element to calculate the temperature derivative and heat flux [54]. The thermal gradient may not be continuous across the boundaries between different elements. Therefore, averaging the results at nodes was needed for data smoothing. Here, the averaging was dependent on the relative nodal variation, which is defined as the ratio (maximum at node – minimum at node) / (maximum over considered region – minimum over considered region). The data averaging was performed only when the relative nodal variation did not exceed 75%.

Fig. 22 shows the role of laser power on cooling rate and thermal gradient in two extreme cases (laser power of 500 and 5500 W, respectively). The cooling rate field in the two cases is presented in Fig. 22a and b, where the grey region with positive values represents the heating region whilst the colour region with negative values represents the cooling region. In both cases, the cooling rate has its maximum value at the top surface behind the melt pool, and it reduces as the region gets further from the melt pool. Fig. 22e shows the cooling rate as a function of temperature on Path 1 and Path 2. The cooling rate increases constantly with the increase of temperature on Path 1, whilst it increases first when the temperature is below 1350 °C and then reduces with the temperature on Path 2. However, for a given path, at the same temperature a higher cooling rate is always observed at a lower laser power (e.g., 800 °C/s for the 500 W case and 400 °C/s for the 5500 W case at 1500 °C on Path 1). Fig. 22c and d show the thermal gradient field in the two cases. The maximum thermal gradient occurs at the bottom of the fusion boundary, and the thermal gradient decreases at a further distance from the melt pool. Fig. 22f shows the thermal gradient as a function of temperature on Path 1 and Path 2. On both paths, the thermal gradient increases with the increase of temperature. Also, at the same temperature a higher thermal gradient is always achieved at a lower laser power.

Fig. 23 shows the effect of the travel speed on the cooling rate and thermal gradient. It can be seen from Fig. 23a and b that when travel speed is high, more material underneath the heat source does not attain the peak temperature when the heat source
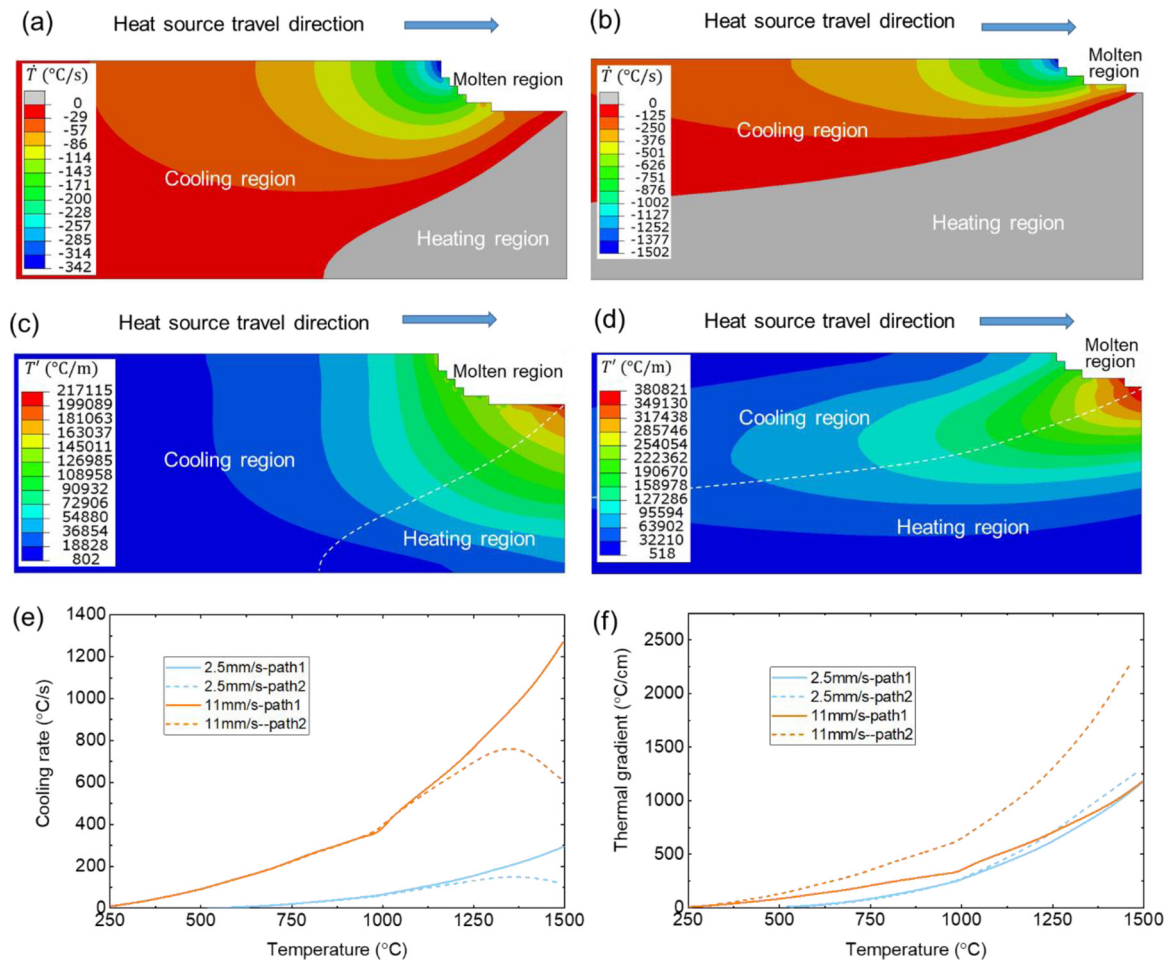
**Fig. 23.** The effect of travel speed on cooling rate and thermal gradient: cooling rate contour at a travel speed of (a) 2.5 mm/s and (b) 11 mm/s; thermal gradient contour at a travel speed of (c) 2.5 mm/s and (d) 11 mm/s; the (e) cooling rate and (f) thermal gradient along Path 1 and Path 2 as a function of temperature.

passes. This is because there is less time for heat to reach these locations compared to the low travel speed case. The maximum cooling rate achieved at the travel speed of 2.5 mm/s is much lower than that at 11 mm/s (342 and 1502 °C/s, respectively). For the thermal gradient in the two cases (Fig. 23c and d), the maximum values are both located at the bottom of the fusion boundary (2171 and 3808 °C/cm, respectively). In addition, one can see from Fig. 23e and f that the trends of the cooling rate and thermal gradient with the increase of temperature on Path 1 and Path 2 are similar as those presented in Fig. 22e and f. Also, the increase of laser power has a similar effect as the decrease of travel speed. By comparing Fig. 22a, b and Fig. 23a, b, or by comparing Fig. 22e and e, one can see that changing travel speed is more effective than laser power to control the cooling rate in the PTA-laser hybrid AM.

To demonstrate the reliability of using this model to provide thermal information for metallurgical study, some regions in HAZ obtained with the simulation and experiments in two different cases were compared, as shown in Fig. 24. The regions of interest underwent a peak temperature ranging from 997 °C ($\beta$-transus) to 1655 °C (solidus temperature). The process parameters used for these two cases are from Case 1 and Case 3 in Table 2, respectively. All parameters used for the two cases are the same except travel speed, which is 4.5 mm/s for Case 1 and 6.5 mm/s for Case 3. Fig. 24a and b show the comparison of the upper boundary of the region of interest (i.e., fusion line). One can see that the simulated fusion line matches well with the experimental result in both

cases. Fig. 24c and d show the comparison of the lower boundary of the region ($\beta$-transus isotherm) in the two cases, where the simulated and experimental results also have good agreement. The well predicted upper boundary and lower boundary of the region of interest confirms that the model has high prediction accuracy.

Due to the lower travel speed used in the first case, more energy input was received by the material in this case than in the second case. This leads to a larger region of interest formed in the first case than in the second case, as shown in Fig. 24e and f (the region between the white dashed line and solid line). For Ti-6Al-4V, when the material is heated to a peak temperature between $\beta$-transus and solidus temperature, $\beta$ grains will increase in size [47,48]. Normally, the higher the peak temperature reaches, the larger the grains become. The microscopic images around the mid-width of the cross-section in the region of interest were shown in Fig. 24g and h. In both cases, $\beta$ grains become smaller from fusion line to $\beta$-transus due to the reduced peak temperature that the material underwent. By comparing the two cases, a larger average $\beta$ grain size was obtained at a lower travel speed, which is consistent with the results observed in Ref. [48]. This can be predicted from the thermal cycles that the material experienced. Fig. 25 shows the thermal cycles at 1 mm below the fusion line at the mid-width in the two cases. The peak temperature reached in the first case was 1389 °C compared to 1354 °C in the second case. Also, the dwell time above $\beta$-transus is longer at a travel speed of 4.5 mm/s compared to that at 6.5 mm/s (3.0 s and 4.9 s, respec-
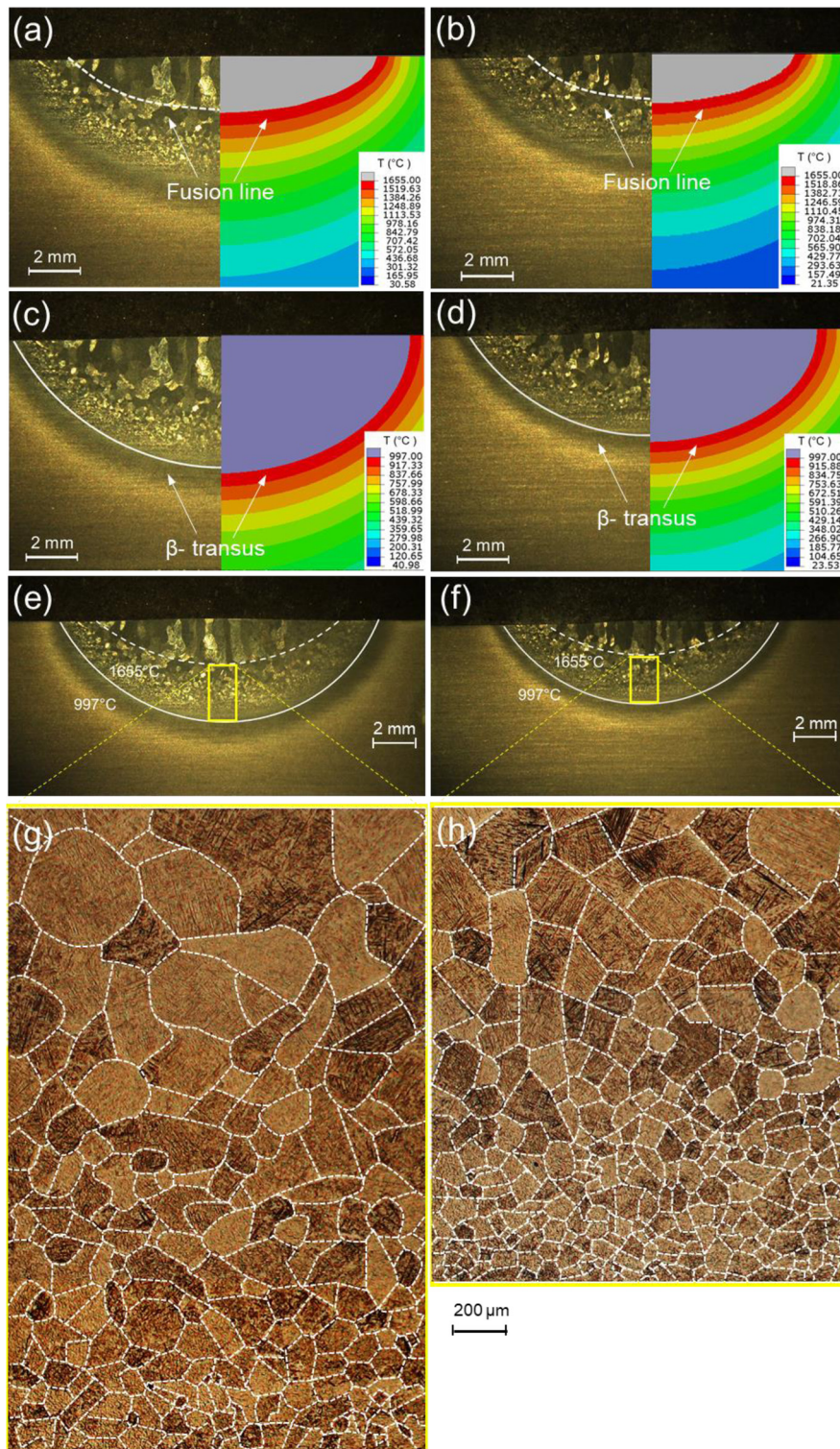
**Fig. 24.** Comparison of HAZ between simulation and experiments at different travel speed: (a) fusion line, (c) $\beta$-transus isotherm, and (e) cross-sectional micrograph at the travel speed of 4.5 mm/s; (b) fusion line, (d) $\beta$-transus isotherm, and (f) cross-sectional micrograph at the travel speed of 6.5 mm/s; (g) grain morphology from the yellow box indicated in (e), and (h) grain morphology from the yellow box indicated in (f).

tively), which gives the grains more time to grow in the former case. This leads to more pronounced grain growth in the first case than that in the second case.

In conduction mode welding or AM, the convection effect in the melt pool is significantly important for heat transfer and melt pool shape formation [55,56], and therefore it cannot be neglected to achieve accurate prediction in a FE model. In a typical FE model

with a volumetric heat source, the energy from the heat source is distributed in a pre-defined volume inside the workpiece. This can be used to achieve an accurate melt pool shape, but it is not physically representative. This is because in conduction mode welding or AM, the energy is transferred from the top surface to the bottom surface of a workpiece. In the proposed model, a surface heat source was used, and artificial conductivity was applied in the melt
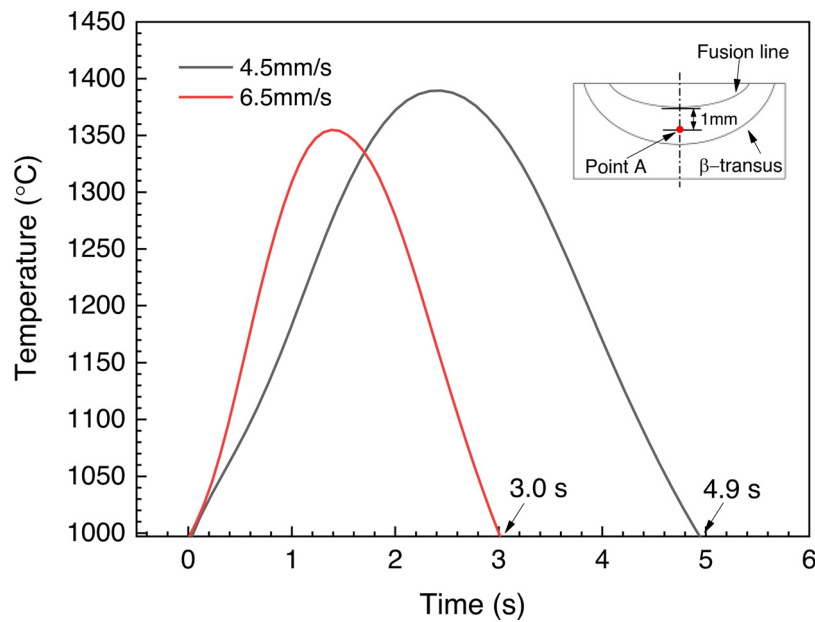
**Fig. 25.** Thermal cycles at a distance of 1mm below the fusion line at mid-width (point A) obtained at two different travel speeds.

pool to compensate for the convection effect thus to achieve accurate melt pool size and shape, which is more physically representative compared to the commonly used volumetric heat source models. In addition, since all the material properties used in the solid state are from the measured values, the thermal filed outside the melt pool can be well predicted. However, the artificial conductivity still cannot completely replace the convection effect in real condition due to the fundamental difference in the heat transfer mode. This means that the temperature distribution in the melt pool cannot be accurately predicted and hence the model should not be used for detailed analysis of thermal variables in the melt pool. In addition, this model is used in the conduction mode. If the operating regime is changed, it might be difficult to calibrate the model to achieve accurate melt pool size and shape. For example, if a very high current or high laser power density is used, in which case the operating regime is very close to or even in the keyhole mode, the proposed model might not be applicable for these conditions.

## 5. Conclusions

In this study, a 3D steady-state FE model with two circular surface heat sources was developed for thermal behaviour analysis in hybrid PTA-laser AM. This model was validated by experimental measurements and its advantages have been demonstrated through comparison with the model with two double ellipsoidal heat sources. The effect of different process parameters, including laser power, travel speed, laser beam size, and arc-laser separation distance, on melt pool geometry and thermal variables was examined using this model. The key findings were summarised as follows.

- The FE model with two circular surface heat sources was calibrated and validated by experiments on melt pool geometry, HAZ boundary, and thermal cycles, which all showed good agreement. Specifically, for the calibration, an average error of 5.8% was obtained for the melt pool (width, length, and depth), and 3.0% for the HAZ (width and depth). For the validation, the average errors for the melt pool and HAZ were 7.3% and 2.2%, respectively.

- The geometric parameters used in the surface heat source model is chosen based on the process, whilst empirical geometric parameters are used in the volumetric heat source model, meaning that the heat source size effect can be captured by the former but not the latter. The melt pool and HAZ geometry in the hybrid process can be predicted accurately using the two circular surface heat sources, whilst accurate melt pool and HAZ cannot be captured using two double ellipsoidal heat sources, meaning that the surface heat source model is more representative for the hybrid process compared to the volumetric heat source model. In addition, compared to the FE model with two double ellipsoidal heat sources, the model with two circular surface heat sources has much fewer parameters required for calibration, meaning that much less effort is needed for the calibration of the surface model.

- For the investigated ranges of all the process parameters, the melt pool geometry depends more strongly on laser power and travel speed compared to arc-laser separation distance and laser beam size. More specifically, the width and depth of the melt pool increase with the increase of laser power and with the decrease of travel speed due to the increased energy input, whilst they are not sensitive to the arc-laser separation distance and laser beam size owing to the unchanged energy input.

- In all the studied cases, the maximum values of cooling rate and thermal gradient are located on the top solidification front and the bottom part of the fusion line, respectively, and both reduce at a further distance from the melt pool. A higher cooling rate and thermal gradient can be achieved using a lower laser power or higher travel speed, and it is more effective to control the cooling rate by changing the travel speed compared to that of laser power. The simulated results and the experimental data showed that the model has high reliability in providing thermal information for metallurgical study.

### Declaration of Competing Interest

The authors declare that they have no known competing financial interests or personal relationships that could have appeared to influence the work reported in this paper.

## CRediT authorship contribution statement

**Chong Wang:** Conceptualization, Methodology, Software, Validation, Formal analysis, Investigation, Data curation, Writing – original draft, Writing – review & editing, Visualization. **Yongle Sun:** Methodology, Formal analysis, Software, Data curation, Writing – review & editing, Visualization. **Guangyu Chen:** Validation, Formal analysis, Investigation, Data curation, Writing – review & editing. **Xin Chen:** Methodology, Validation, Formal analysis, Writing – review & editing, Visualization. **Jialuo Ding:** Conceptualization, Methodology, Formal analysis, Supervision, Writing – review & editing. **Wojciech Suder:** Methodology, Formal analysis, Supervision, Writing – review & editing. **Chenglei Diao:** Validation, Formal analysis, Data curation, Writing – review & editing. **Stewart Williams:** Conceptualization, Methodology, Writing – review & editing, Supervision, Funding acquisition.

## Data Statement

## Acknowledgements

## References

[1] D. Herzog, V. Seyda, E. Wycisk, C. Emmelmann, Additive manufacturing of metals, Acta Mater. 117 (2016) 371–392, doi:10.1016/j.actamat.2016.07.019.

[2] E. Liverani, S. Toschi, L. Ceschini, A. Fortunato, Effect of selective laser melting (SLM) process parameters on microstructure and mechanical properties of 316L austenitic stainless steel, J. Mater. Process. Technol. 249 (2017) 255–263, doi:10.1016/j.jmatprotec.2017.05.042.

[3] E. Brandl, F. Palm, V. Michailov, B. Viehweger, C. Leyens, Mechanical properties of additive manufactured titanium (Ti-6Al-4V) blocks deposited by a solid-state laser and wire, Mater. Des. 32 (2011) 4665–4675, doi:10.1016/j.matdes.2011.06.062.

[4] M. Galati, L. Iuliano, A literature review of powder-based electron beam melting focusing on numerical simulations, Addit. Manuf. 19 (2018) 1–20, doi:10.1016/j.addma.2017.11.001.

[5] R. Hu, X. Chen, G. Yang, S. Gong, S. Pang, Metal transfer in wire feeding-based electron beam 3D printing: modes, dynamics, and transition criterion, Int. J. Heat Mass Transf. 126 (2018) 877–887, doi:10.1016/j.ijheatmasstransfer.2018.06.033.

[6] Z. Qi, B. Cong, B. Qi, H. Sun, G. Zhao, J. Ding, Microstructure and mechanical properties of double-wire + arc additively manufactured Al-Cu-Mg alloys, J. Mater. Process. Technol. 255 (2018) 347–353, doi:10.1016/j.jmatprotec.2017.12.019.

[7] C. Wang, W. Suder, J. Ding, S. Williams, The effect of wire size on high deposition rate wire and plasma arc additive manufacture of Ti-6Al-4V, J. Mater. Process. Technol. 288 (2021) 116842, doi:10.1016/j.jmatprotec.2020.116842.

[8] B. Cong, J. Ding, S. Williams, Effect of arc mode in cold metal transfer process on porosity of additively manufactured Al-6.3%Cu alloy, Int. J. Adv. Manuf. Technol. 76 (2015) 1593–1606, doi:10.1007/s00170-014-6346-x.

[9] C. Wang, W. Suder, J. Ding, S. Williams, Wire based plasma arc and laser hybrid additive manufacture of Ti-6Al-4V, J. Mater. Process. Technol. 293 (2021) 117080, doi:10.1016/j.jmatprotec.2021.117080.

[10] C. Wang, W. Suder, J. Ding, S. Williams, Bead shape control in wire based plasma arc and laser hybrid additive manufacture of Ti-6Al-4V, J. Manuf. Process. 68 (2021) 1849–1859, doi:10.1016/j.jmapro.2021.07.009.

[11] J. Gockel, J. Beuth, K. Taminger, Integrated control of solidification microstructure and melt pool dimensions in electron beam wire feed additive manufacturing of ti-6al-4v, Addit. Manuf. 1 (2014) 119–126, doi:10.1016/j.addma.2014.09.004.

[12] J. Xiong, Y. Lei, R. Li, Finite element analysis and experimental validation of thermal behavior for thin-walled parts in GMAW-based additive manufacturing with various substrate preheating temperatures, Appl. Therm. Eng. 126 (2017) 43–52, doi:10.1016/j.applthermaleng.2017.07.168.

[13] J. Li, Z. Wei, L. Yang, B. Zhou, Y. Wu, S.G. Chen, Z. Sun, Finite element analysis of thermal behavior and experimental investigation of Ti6Al4V in selective laser melting, Optik (Stuttg) 207 (2020) 163760, doi:10.1016/j.ijleo.2019.163760.

[14] Y. Chen, H. Chen, J.Q. Chen, J. Xiong, Y. Wu, S.Y. Dong, Numerical and experimental investigation on thermal behavior and microstructure during selective laser melting of high strength steel, J. Manuf. Process. 57 (2020) 533–542, doi:10.1016/j.jmapro.2020.06.041.

[15] Y. Li, D. Gu, Parametric analysis of thermal behavior during selective laser melting additive manufacturing of aluminum alloy powder, Mater. Des. 63 (2014) 856–867, doi:10.1016/j.matdes.2014.07.006.

[16] J. Ding, P. Colegrove, J. Mehnen, S. Ganguly, P.M.S. Almeida, F. Wang, S. Williams, Thermo-mechanical analysis of wire and arc additive layer manufacturing process on large multi-layer parts, Comput. Mater. Sci. 50 (2011) 3315–3322, doi:10.1016/j.commatsci.2011.06.023.

[17] B. Acherjee, Hybrid laser arc welding: state-of-art review, Opt. Laser Technol. 99 (2018) 60–71, doi:10.1016/j.optlastec.2017.09.038.

[18] X. Chen, Z. Mu, R. Hu, L. Liang, A.B. Murphy, S. Pang, A unified model for coupling mesoscopic dynamics of keyhole, metal vapor, arc plasma, and weld pool in laser-arc hybrid welding, J. Manuf. Process. 41 (2019) 119–134, doi:10.1016/j.jmapro.2019.03.034.

[19] B. Ribic, R. Rai, T. DebRoy, Numerical simulation of heat transfer and fluid flow in GTA/Laser hybrid welding, Sci. Technol. Weld. Join. 13 (2008) 683–693, doi:10.1179/136217108X356782.

[20] X. Cai, H. Li, H. Wei, L. Yang, Y. Gao, Effect of laser on the welding process of short-circuiting transfer MIG welding of aluminum alloys, Int. J. Adv. Manuf. Technol. 75 (2014) 1829–1836, doi:10.1007/s00170-014-6250-4.

[21] L. Chen, G. Mi, X. Zhang, C. Wang, Numerical and experimental investigation on microstructure and residual stress of multi-pass hybrid laser-arc welded 316L steel, Mater. Des. 168 (2019) 107653, doi:10.1016/j.matdes.2019.107653.

[22] F. Kong, J. Ma, R. Kovacevic, Numerical and experimental study of thermally induced residual stress in the hybrid laser-GMA welding process, J. Mater. Process. Technol. 211 (2011) 1102–1111, doi:10.1016/j.jmatprotec.2011.01.012.

[23] G. Chen, S. Williams, J. Ding, Y. Wang, W. Suder, Split anode calorimetry for plasma arc energy density measurement with laser calibration, J. Manuf. Process. 78 (2022) 71–81, doi:10.1016/j.jmapro.2022.04.003.

[24] V.D. Fachinotti, A. Cardona, B. Baufeld, O. Van Der Biest, Finite-element modelling of heat transfer in shaped metal deposition and experimental validation, Acta Mater. 60 (2012) 6621–6630, doi:10.1016/j.actamat.2012.08.031.

[25] A. Askari, S. Das, Practical numerical analysis of a crack near a weld subjected to primary loading and hydrogen embrittlement, J. Mater. Process. Technol. 173 (2006) 1–13, doi:10.1016/j.jmatprotec.2004.12.005.

[26] Y.L. Sun, G. Obasi, C.J. Hamelin, A.N. Vasileiou, T.F. Flint, J. Balakrishnan, M.C. Smith, J.A. Francis, Effects of dilution on alloy content and microstructure in multi-pass steel welds, J. Mater. Process. Technol. 265 (2019) 71–86, doi:10.1016/j.jmatprotec.2018.09.037.

[27] A. Mahrle, J. Schmidt, Numerical simulation of heat transfer during deep penetration laser beam welding, Proc. Int. Conf. Adv. Comput. Methods Heat Transf. 20 (1998) 233–242 https://www.witpress.com/elibrary/wit-transactions-on-engineering-sciences/20/6588.

[28] J. Goldak, A. Chakravarti, M. Bibby, A new finite element model for welding heat sources, Metall. Trans. B 15B (1984) 299–305, doi:10.1007/BF02667333.

[29] J. Ahn, E. He, L. Chen, R.C. Wimpory, J.P. Dear, C.M. Davies, Prediction and measurement of residual stresses and distortions in fibre laser welded Ti-6Al-4V considering phase transformation, Mater. Des. 115 (2017) 441–457, doi:10.1016/j.matdes.2016.11.078.

[30] R. Boyer, G. Welsch, E.G. Collings, Materials Properties Handbook: Titanium Alloys, ASM International, Materials Park, 1994 https://books.google.co.uk/books?hl=en&lr=&id=x3rToHWOcD8C&oi=fnd&pg=PP23&dq=Materials+properties+handbook&ots=x7y0MF8re_&sig=uqkCbkTAjVltY1NtVRiwXo14tkg&redir_esc=y#v=onepage&q=Materials%20properties%20handbook&f=false.

[31] A.B. Murphy, J.J. Lowke, in: Heat Transfer in ARC Welding. Handbook of Thermal Science and Engineering, Springer International Publishing, 2018, pp. 2657–2727. https://link.springer.com/referenceworkentry/10.1007/978-3-319-26695-4_29.

[32] A. Ebrahimi, M. Sattari, S.J.L. Bremer, M. Luckabauer, G. willem, R.B.E. Römer, I.M. Richardson, C.R. Kleijn, M.J.M. Hermans, The influence of laser characteristics on internal flow behaviour in laser melting of metallic substrates, Mater. Des. (2022) 214, doi:10.1016/j.matdes.2022.110385.

[33] G. Zhang, G. Goett, R. Kozakov, D. Uhrlandt, U. Reisgen, K. Willms, R. Sharma, S. Mann, P. Lozano, Study of the arc voltage in gas metal arc welding, J. Phys. D. Appl. Phys. 52 (2018) 085202, doi:10.1088/1361-6463/aaf588.

[34] H.S. Tran, J.T. Tchuindjang, H. Paydas, A. Mertens, R.T. Jardin, L. Duchêne, R. Carrus, J. Lecomte-Beckers, A.M. Habraken, 3D thermal finite element analysis of laser cladding processed Ti-6Al-4V part with microstructural correlations, Mater. Des. 128 (2017) 130–142, doi:10.1016/j.matdes.2017.04.092.

[35] S.A. Tsirkas, P. Papanikos, T. Kermanidis, Numerical simulation of the laser welding process in butt-joint specimens, J. Mater. Process. Technol. 134 (2003) 59–69, doi:10.1016/S0924-0136(02)00921-4.

[36] P. Dai, Y. Wang, S. Li, S. Lu, G. Feng, D. Deng, FEM analysis of residual stress induced by repair welding in SUS304 stainless steel pipe butt-welded joint, J. Manuf. Process. 58 (2020) 975–983, doi:10.1016/j.jmapro.2020.09.006.

[37] P.W. Fuerschbach, G.A. Knorovsky, A study of melting efficiency in plasma arc and gas tungsten arc welding, Weld. J. 70 (11) (1991) 287s–297s https://app.aws.org/wj/supplement/WJ_1991_11_s287.pdf.

[38] H. Kwon, W.K. Baek, M.S. Kim, W.S. Shin, J.J. Yoh, Temperature-dependent absorptance of painted aluminum, stainless steel 304, and titanium for 1.07 $\mu$m and 10.6 $\mu$m laser beams, Opt. Lasers Eng. 50 (2012) 114–121, doi:10.1016/j.optlaseng.2011.10.001.

[39] C.D. Boley, S.A. Khairallah, A.M. Rubenchik, Calculation of laser absorption by metal powders in additive manufacturing, Appl. Opt. 54 (2015) 2477–2482, doi:10.1364/AO.54.002477.

[40] C.D. Boley, S.C. Mitchell, A.M. Rubenchik, S.S.Q. Wu, Metal powder absorptivity: modeling and experiment, Appl. Opt. 55 (2016) 6496, doi:10.1364/ao.55.006496.

[41] F. Lia, J. Park, J. Tressler, R. Martukanitz, Partitioning of laser energy during directed energy deposition, Addit. Manuf. 18 (2017) 31–39, doi:10.1016/j.addma.2017.08.012.

[42] W. Ou, T. Mukherjee, G.L. Knapp, Y. Wei, T. DebRoy, Fusion zone geometries, cooling rates and solidification parameters during wire arc additive manufacturing, Int. J. Heat Mass Transf. 127 (2018) 1084–1094, doi:10.1016/j.ijheatmasstransfer.2018.08.111.

[43] X. Bai, P. Colegrove, J. Ding, X. Zhou, C. Diao, P. Bridgeman, J. Roman Hönnige, H. Zhang, S. Williams, Numerical analysis of heat transfer and fluid flow in multilayer deposition of PAW-based wire and arc additive manufacturing, Int. J. Heat Mass Transf. 124 (2018) 504–516, doi:10.1016/j.ijheatmasstransfer.2018.03.085.

[44] T. Fuhrich, P. Berger, H. Hügel, Marangoni effect in laser deep penetration welding of steel, J. Laser Appl. 13 (2001) 178–186, doi:10.2351/1.1404412.

[45] A. Ebrahimi, C.R. Kleijn, M.J.M. Hermans, I.M. Richardson, The effects of process parameters on melt-pool oscillatory behaviour in gas tungsten arc welding, J. Phys. D Appl. Phys. 54 (2021), doi:10.1088/1361-6463/abf808.

[46] L. Aucott, H. Dong, W. Mirihanage, R. Atwood, A. Kidess, S. Gao, S. Wen, J. Marsden, S. Feng, M. Tong, T. Connolley, M. Drakopoulos, C.R. Kleijn, I.M. Richardson, D.J. Browne, R.H. Mathiesen, H.V. Atkinson, Revealing internal flow behaviour in arc welding and additive manufacturing of metals, Nat. Commun. 9 (2018) 1–7, doi:10.1038/s41467-018-07900-9.

[47] E. Brandl, V. Michailov, B. Viehweger, C. Leyens, Deposition of Ti-6Al-4V using laser and wire, part I: microstructural properties of single beads, Surf. Coat. Technol. 206 (2011) 1120–1129, doi:10.1016/j.surfcoat.2011.07.095.

[48] S. Mishra, T. DebRoy, Measurements and Monte Carlo simulation of grain growth in the heat-affected zone of Ti-6Al-4V welds, Acta Mater. 52 (2004) 1183–1192, doi:10.1016/j.actamat.2003.11.003.

[49] D. Deng, H. Murakawa, Prediction of welding distortion and residual stress in a thin plate butt-welded joint, Comput. Mater. Sci. 43 (2008) 353–365, doi:10.1016/j.commatsci.2007.12.006.

[50] X. Li, L. Wang, L. Yang, J. Wang, K. Li, Modeling of temperature field and pool formation during linear laser welding of DP1000 steel, J. Mater. Process. Technol. 214 (2014) 1844–1851, doi:10.1016/j.jmatprotec.2014.03.030.

[51] N. Siva Shanmugam, G. Buvanashekaran, K. Sankaranarayanasamy, Some studies on weld bead geometries for laser spot welding process using finite element analysis, Mater. Des. 34 (2012) 412–426, doi:10.1016/j.matdes.2011.08.005.

[52] J. Wang, J. Han, J.P. Domblesky, Z. Yang, Y. Zhao, Q. Zhang, Development of a new combined heat source model for welding based on a polynomial curve fit of the experimental fusion line, Int. J. Adv. Manuf. Technol. 87 (2016) 1985–1997, doi:10.1007/s00170-016-8587-3.

[53] T. Ahmed, H.J. Rack, Phase transformations during cooling in $\alpha + \beta$ titanium alloys, Mater. Sci. Eng. A. 243 (1998) 206–211, doi:10.1016/s0921-5093(97)00802-2.

[54] Dassault Systems: Abaqus, 2019 Documentation. https://www.3ds.com/support/documentation/.

[55] A. Ebrahimi, C.R. Kleijn, I.M. Richardson, Numerical study of molten metal melt pool behaviour during conduction-mode laser spot melting, J. Phys. D. Appl. Phys. (2021) 54, doi:10.1088/1361-6463/abca62.

[56] G. Ehlen, A. Ludwig, P.R. Sahm, Simulation of time-dependent pool shape during laser spot welding: transient effects, Metall. Mater. Trans. A Phys. Metall. Mater. Sci. 34 (2003) 2947–2961, doi:10.1007/s11661-003-0194-x.

2022-06-25

# A simplified modelling approach for thermal behaviour analysis in hybrid plasma arc-laser additive manufacturing

Wang, Chong

Elsevier